Tutorial

James N. Hilfiker*, Nina Hong and Stefan Schoeche

Mueller matrix spectroscopic ellipsometry

https://doi.org/10.1515/aot-2022-0008
Received March 15, 2022; accepted May 4, 2022;
published online June 7, 2022

Abstract: The Mueller matrix is a mathematical description of how light is altered by an optical element or a sample under study. It describes both intensity (irradiance) and polarization changes, including a reduction of the total polarization. Mueller matrix spectroscopic ellipsometry has gained recent popularity in the optics and semiconductor communities as an effective means to characterize complex sample structures and anisotropic materials. While this method is not new, its recent expansion to new fields has left many users with only a pedestrian understanding of the data they collect. This tutorial provides an overview of Mueller matrix spectroscopic ellipsometry with focus on practical aspects for those new to the technique.

Keywords: ellipsometry; Mueller matrix; polarimetry; polarization; thin film optical properties.

1 Introduction

The Mueller matrix (**M**) is a real-valued 4 × 4 matrix developed in 1943 by Swiss–American physicist Hans Mueller (1900–1965). It describes an optical system (or, in our case, a sample of interest) in terms of experimentally observable quantities and connects the input and output real-valued 4 × 1 Stokes vectors (**S**) describing light as given by:

$$\mathbf{S}_{\text{out}} = \mathbf{M}\mathbf{S}_{\text{in}} \quad (1)$$

Hans Mueller used the matrix calculation in his lecture at the Massachusetts Institute of Technology, but it was not published for general use at that time [1]. Mueller's algebra was later introduced to the public by his student, N. G. Parke, in his dissertation [2] and paper [3]. It is believed that the name 'Mueller matrix (MM)' was first coined by Parke. Notice that it took almost a century from the time Stokes (1819–1903) developed the Stokes vector in 1852 [4, 5] until Mueller took the theory and established a complete expression for the polarized light and matter interaction. In fact, lesser known are French scientists Paul Soleillet [6] and Francis Perrin [7], who established a similar mathematical formalism based on Stokes vectors before Mueller.

One of the scientific significances of the Mueller calculus is that the algebra uses real-valued elements as opposed to the Jones calculus [8]. The Jones vector describes the polarization ellipse of an electric field in terms of complex numbers related to amplitudes and phases; thus, it is only applicable to completely polarized light and impractical to directly measure at optical frequencies. On the other hand, the Mueller calculus can describe an optical system directly related to measurable intensities. Because Stokes vectors apply to both partially and fully polarized light, the MM contains information about depolarization caused by the optical element. The experimental convenience of the Mueller calculus has led to extensive theoretical research efforts to find the constraints on Mueller matrices that are physically realizable or non-depolarizing [9–12]. For depolarizing Mueller matrices, various methods have been developed to quantify the degree of polarization or depolarization [13–15]. Another practical index is the Jones matrix quality factor describing the difference between the measured MM and a best-matching, non-depolarizing MM calculated from a Jones matrix. This index is applicable even for partial Mueller matrices [16].

Common MM measurement techniques are MM polarimetry [17–19], MM spectroscopic ellipsometry (MMSE) [20–24], and MM imaging [25–31]. Both MM polarimetry and MMSE measure the MM of a sample in reflection or transmission using a polarization state generator and a polarization state analyzer, the difference being that polarimetry usually determines the MM from a set of fixed, defined polarization configurations whereas MMSE exposes the sample to many different polarization states and detects many different polarization states by continuously modulating the polarizing optical elements. In other words, MM polarimetry measures absolute intensities

***Corresponding author: James N. Hilfiker**, J.A. Woollam Company, 311 South 7th St., Lincoln, NE, 68508, USA,
E-mail: jhilfiker@jawoollam.com. https://orcid.org/0000-0002-4874-5429
Nina Hong and Stefan Schoeche, J.A. Woollam Company, 311 South 7th St., Lincoln, NE, 68508, USA

Open Access. © 2022 James N. Hilfiker et al., published by De Gruyter. This work is licensed under the Creative Commons Attribution 4.0 International License.

whereas MMSE measures relative polarization changes and does not rely on determining absolute intensity values. MMSE extends its use through modeling to measure film thickness and index of refraction, mainly on stratified media [32]. MM imaging combines MM polarimetry or MMSE with imaging techniques [33].

MM measurement techniques are used in a variety of applications because of their general suitability to measure many sample types. The MM of anisotropic samples enables access to intriguing optical properties such as the birefringence or dichroism of flexible polymeric substrates [34, 35], the retardance and tilt distribution of liquid crystals [36–39], the anisotropic optical constants and dimensional parameters of nanostructured thin films or metamaterials [40–48], and the 3×3 dielectric tensor and Euler angles of low symmetry crystals [49–54]. MM data has been used to reconstruct the optical critical dimensions of diffraction gratings formed by integrated circuit devices [55–60]. Biomedical applications include the polarizing phenomena of photonic structures found in beetles [61, 62] or butterflies [63] and obtaining polarization images of biological tissues [64].

There are many excellent books and articles that provide the mathematical details of the MM [15, 33, 48, 65–67]. However, it can be difficult to compress this information to a level needed by those using MMSE for their sample characterization. They need to understand what data is contained in the MM and how it can be used to extract relevant sample properties. The focus of this tutorial is to provide a concise introduction to the topic without overwhelming a novice user. We begin with a brief mathematical description. More important, we discuss the meaning of the MM elements and the corresponding sections related to light attenuation, diattenuation, polarizance, and retardance. There is often a great deal of "duplicate information" within the MM, such that many samples can be characterized with only a subset of the full MM. We describe a few common measurement configurations and which MM elements they can access. We continue to describe common samples that may be encountered and how their physical attributes manifest in different MM shapes. One of the key capabilities of the MM is that it can handle depolarizing samples, so we devote a section to depolarization and its causes.

The MM can be used at different levels. At the most basic, the MM represents a transfer-function for light under the same conditions as the measurement. This transfer-function can be used directly in optical modeling of a "device" but does not provide predictive capabilities or access to deeper understanding of the sample/material properties. Several well-known MM decomposition methods [12, 68–75] are described that can access the phenomenological quantities of the sample. For a deeper understanding, the MM can be modeled using Fresnel-based calculations [65, 76, 77] or even rigorous coupled wave analysis (RCWA) [78–80] to fit the underlying material and structural properties or subwavelength critical dimensions in periodic samples. This tutorial concludes with a few brief applications to demonstrate the diverse areas in which MMSE is used. These examples demonstrate the current state-of-the-art for what is possible by skilled users in the field.

2 Mathematical overview

An MM describes any optical element, or in our case the sample under study, that modifies the properties of light. Figure 1 shows a measurement system, where (left-to-right) unpolarized light enters a rotating optical element, is reflected from a sample, travels through a fixed-position optical element and is then detected. Stokes vectors are used to describe the properties of light at any point along this path. An MM is used to describe how each optical element, or the sample, alters the light. The MM is general enough to describe how any potential light beam will be altered. In this section, we introduce the Mueller–Stokes algebra.

Spectroscopic ellipsometry (SE) measures the polarization change that occurs when polarized light interacts (reflection or transmission) with a sample of interest [65, 76]. When referring to ellipsometry measurements, it is common to differentiate between electric fields that are vibrating parallel to the plane of incidence (p-polarized) and those perpendicular to the plane of incidence (s-polarized), as shown in Figure 2. The measured quantity in so-called "Standard SE" is a complex number $\tilde{\rho}$ typically

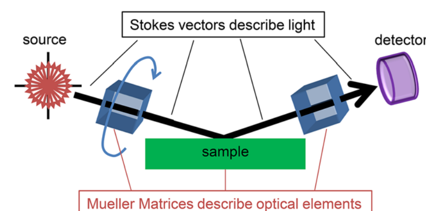

Figure 1: Ellipsometry measurement setup with unpolarized source light traveling through a rotating optical element, reflecting from a sample at oblique angle of incidence, continuing through a fixed optical element, and arriving at a detector. Stokes vectors can describe the light properties at each point along this optical path, whereas an MM can describe the transformation of light by each optical element and the sample under study.

expressed in terms of two parameters, Ψ and Δ, related to the ratio of the *p*- and *s*- polarized sample interaction:

$$\tilde{\rho} = \tan \Psi e^{i\Delta} = \frac{\tilde{R}_p}{\tilde{R}_s} \quad (2)$$

where $\tilde{R}_p$ and $\tilde{R}_s$ are the complex total reflection coefficients. Here, Ψ is related to the amplitude ratio and Δ is related to a phase difference between *p*- and *s*-polarized light resulting from interaction with the sample.

Standard SE measurements are typically used to characterize isotropic materials, i.e. those with the same optical properties for light polarized in any direction. Anisotropic materials, with different optical properties for different polarization directions, require more advanced measurements such as generalized spectroscopic ellipsometry or MMSE. Generalized spectroscopic ellipsometry measurements determine the normalized Jones matrix including cross-polarization, i.e. mixed output polarization states for a pure *p*- or *s*-input polarization state, which often occurs when measuring anisotropic samples [65]. However, MMSE measurements are the most general ellipsometry measurement type, not only providing access to cross-polarization but also being applicable to depolarizing samples – where the detected light is no longer completely polarized. Section 6 in this tutorial is dedicated to phenomena which involve depolarization.

The Mueller matrix is a 4 × 4 matrix describing the transformation from incoming to outgoing Stokes vectors, as:

$$\begin{pmatrix} S'_0 \\ S'_1 \\ S'_2 \\ S'_3 \end{pmatrix}_{\text{out}} = \begin{bmatrix} M_{11} & M_{12} & M_{13} & M_{14} \\ M_{21} & M_{22} & M_{23} & M_{24} \\ M_{31} & M_{32} & M_{33} & M_{34} \\ M_{41} & M_{42} & M_{43} & M_{44} \end{bmatrix} \cdot \begin{pmatrix} S_0 \\ S_1 \\ S_2 \\ S_3 \end{pmatrix}_{\text{in}} \quad (3)$$

The Stokes vector (often called Stokes parameters as it is not a true vector but rather a column matrix) describes light with four intensity measurements for different polarizations as:

$$\mathbf{S} = \begin{bmatrix} S_0 \\ S_1 \\ S_2 \\ S_3 \end{bmatrix} = \begin{bmatrix} I_x + I_y \\ I_x - I_y \\ I_{+45°} - I_{-45°} \\ I_R - I_L \end{bmatrix} \quad (4)$$

where I_x, I_y, I_{+45}, and I_{-45} are the intensities of linearly polarized light oriented along the *x*, *y*, +45°, and −45° directions, respectively; and I_R and I_L are the intensities of *right* and *left* circular polarizations, respectively. The *x* and *y* orientations are often matched to the measurement coordinate system, which in the case of MMSE are the *p* and *s* polarization directions for the sample.

Before proceeding further, it is important to note the conventions used within this paper. We will be following what is referred to as the "Nebraska Convention" by the ellipsometry community [65, 81]. As such, the time dependence of the electric-field oscillation will be:

$$E \sim \exp(i\omega t) \quad (5)$$

and the rotation of the electric field for elliptical or circular polarization is determined by watching the electric field at a fixed location looking toward the source of light. If the electric field rotates clockwise, it is referred to as "right" circular or elliptical, whereas counterclockwise is referred to as "left" circular or elliptical.

As shown in Figure 3, the MM describes the transformation of light upon interaction with an optical element (which we will now refer to as our sample under study). The MM can describe how light is altered upon reflection or after transmission through the sample. While the MM describes the properties of the sample regardless of the incoming light properties, it only describes the sample under the same measurement conditions – reflection or transmission at a specific angle of incidence.

Both Stokes vectors and Mueller matrices are often normalized to retain the polarization-dependent information irrespective of absolute intensity. We use lowercase

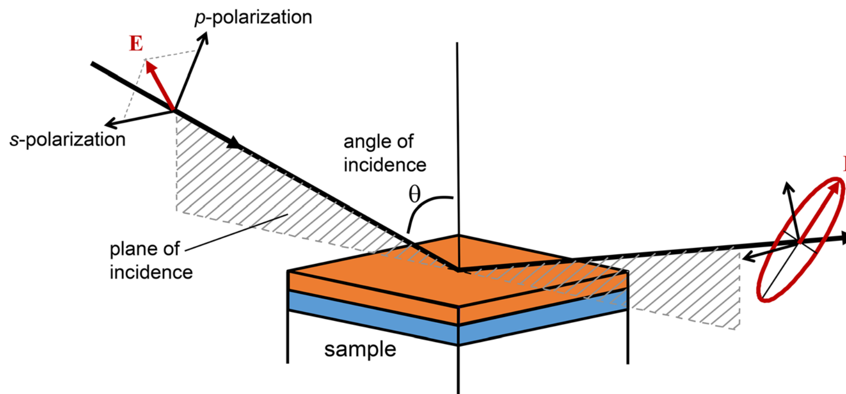

Figure 2: Ellipsometry measurement at an oblique angle, θ. The plane of incidence contains the incident light, the reflected light, and the sample normal. The *p*-polarized and *s*-polarized electric fields are vibrating parallel and perpendicular to the plane of incidence, respectively, and form a frame of reference for the electric field polarizations. Linearly polarized incident light with both *p*- and *s*-components will most generally become elliptically polarized light upon reflection.

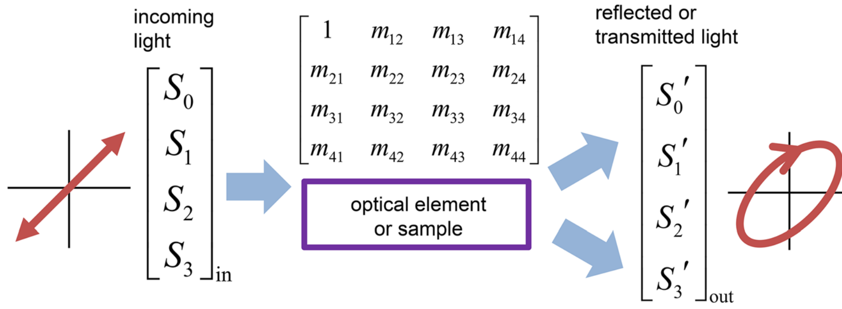

Figure 3: The transformation of light (as described by a Stokes vector) by an optical element or sample under study can be described by an MM. This transformation may result from transmission through or reflection from the optic/sample in question. The MM is valid for a specific measurement configuration but can describe the transformation of any incoming light beam.

elements for normalized Stokes parameters (Eq. (6)) and normalized Mueller matrices (Eq. (7)).

$$\begin{bmatrix} S_0/S_0 \\ S_1/S_0 \\ S_2/S_0 \\ S_3/S_0 \end{bmatrix} = \begin{bmatrix} 1 \\ s_1 \\ s_2 \\ s_3 \end{bmatrix} \tag{6}$$

$$\begin{bmatrix} 1 & m_{12} & m_{13} & m_{14} \\ m_{21} & m_{22} & m_{23} & m_{24} \\ m_{31} & m_{32} & m_{33} & m_{34} \\ m_{41} & m_{42} & m_{43} & m_{44} \end{bmatrix}, \text{where } m_{ij} = \frac{M_{ij}}{M_{11}} \tag{7}$$

Because we normalize to the total intensity, the remaining Stokes parameters are restricted between ±1. Similarly, the normalized MM elements, m_{ij}, are constrained between ±1. We will consider the general shapes of MM for common optical elements in a later section. A few common normalized Stokes vectors are shown in Table 1.

When intensity information is desired, an unnormalized MM can be measured. This is the only situation that requires the absolute intensity of light to be determined in an MMSE measurement while all other MM elements are determined from the relative polarization change and independent of absolute intensity levels. In this tutorial, any unnormalized MM will still be written in normalized form, but with the M_{11} value retained:

$$M_{11} \begin{bmatrix} 1 & m_{12} & m_{13} & m_{14} \\ m_{21} & m_{22} & m_{23} & m_{24} \\ m_{31} & m_{32} & m_{33} & m_{34} \\ m_{41} & m_{42} & m_{43} & m_{44} \end{bmatrix} \tag{8}$$

M_{11} is often misinterpreted as describing the reflectance or transmittance of a sample. However, M_{11} only describes the reflected or transmitted intensity for unpolarized light. The actual reflectance or transmittance depends on the incoming polarization state and the entire first row of the MM. The measured intensity will also depend on the type of detection – is it considering the intensity of all transmitted/reflected polarization states or just a specific polarization direction. When M_{11} is measured, we can calculate the transmitted or reflected polarized intensities (I_{ij}) for any *like* or *crossed* polarizations, where *i* is the incoming polarization direction and *j* is the detected polarization direction:

$$I_{pp} = \frac{M_{11}\,(1 + m_{12} + m_{21} + m_{22})}{2} \tag{9a}$$

Table 1: Example normalized Stokes vectors for common polarization states of light.

Polarization	Normalized stokes vector
Linear *x*-polarized light	$\begin{bmatrix} 1 \\ 1 \\ 0 \\ 0 \end{bmatrix}$
Linear *y*-polarized light	$\begin{bmatrix} 1 \\ -1 \\ 0 \\ 0 \end{bmatrix}$
Linear +45° polarized light	$\begin{bmatrix} 1 \\ 0 \\ 1 \\ 0 \end{bmatrix}$
Linear −45° polarized light	$\begin{bmatrix} 1 \\ 0 \\ -1 \\ 0 \end{bmatrix}$
Right circularly polarized light	$\begin{bmatrix} 1 \\ 0 \\ 0 \\ 1 \end{bmatrix}$
Left circularly polarized light	$\begin{bmatrix} 1 \\ 0 \\ 0 \\ -1 \end{bmatrix}$
Unpolarized light	$\begin{bmatrix} 1 \\ 0 \\ 0 \\ 0 \end{bmatrix}$

$$I_{ss} = \frac{M_{11}\,(1 - m_{21} - m_{12} + m_{22})}{2} \tag{9b}$$

$$I_{ps} = \frac{M_{11}\,(1 - m_{21} + m_{12} - m_{22})}{2} \tag{9c}$$

$$I_{sp} = \frac{M_{11}\,(1 + m_{21} - m_{12} - m_{22})}{2} \tag{9d}$$

Figure 4 compares M_{11} to the polarized reflectance from a bare silicon substrate versus angle of incidence. In this case the M_{11} value can either be larger or smaller than the measured reflectance depending on the polarization of the incoming light wave. This is resolved by the fact that the normalized MM elements can be positive or negative (bounded by ±1). A single reflection from a substrate will have a negative m_{12} value, which will remain negative when multiplied by an incoming *p*-polarization – reducing the intensity of the outgoing light (compared to M_{11}) and resulting in the expected minimum of *p*-polarized reflectance, R_p, at the Brewster angle.

One hurdle to using the Mueller matrix is understanding what an individual MM element represents. Each MM element maps one input property of light (MM column) to one output property of light (MM row). It shows if and how a certain light polarization will be altered based on specific incoming light properties. We demonstrate this concept using the M_{23} element in Figure 5. This single element will only influence incoming light that contains a linear polarization component oriented at ± 45° (described by S_2 of the incoming light). If the incoming light contains ±45° polarization, the m_{23} element will describe how that light may be altered to form linearly polarized light along the *x*/*y* directions (described by S_1' of the outgoing light). The overall description for the outgoing *x*/*y* polarization properties, described by S_1' will also depend on the entire second row of the MM and the incoming light properties, as shown in Figure 5. In this manner, each MM element is only a single piece of the overall puzzle.

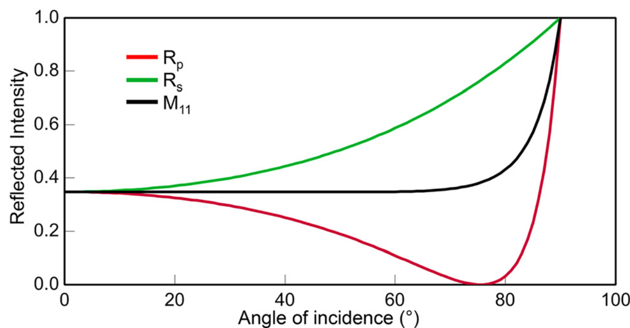

Figure 4: The reflectance for *p*- and *s*- polarized light compared to M_{11} versus angle of incidence simulated from a bare silicon surface.

$$\begin{bmatrix} S_0' \\ S_1' \\ S_2' \\ S_3' \end{bmatrix}_{out} = \begin{bmatrix} M_{11} & M_{12} & M_{13} & M_{14} \\ M_{21} & M_{22} & M_{23} & M_{24} \\ M_{31} & M_{32} & M_{33} & M_{34} \\ M_{41} & M_{42} & M_{43} & M_{44} \end{bmatrix} \cdot \begin{bmatrix} S_0 \\ S_1 \\ S_2 \\ S_3 \end{bmatrix}_{in}$$

$$S_1' = M_{21}S_0 + M_{22}S_1 + M_{23}S_2 + M_{24}S_3$$

Figure 5: Visual representation of a single MM element and how it relates specific incoming light properties to specific outgoing light properties.

3 Sections of the Mueller matrix

Different sample properties will populate different elements of the MM. Thus, it can be helpful to understand the general MM "shapes" that may be encountered, i.e. which groups of MM elements are populated for different samples. We start by separating the MM into four sections shown in Figure 6: unpolarized attenuation (gray), diattenuation (red), polarizance (blue), and retardance (yellow).

The M_{11} value describes the attenuation of outgoing intensity for an unpolarized input light beam, or the contribution to attenuation for the outgoing intensity from the unpolarized portion of the incoming light beam. When the incoming light beam is completely unpolarized the S_1, S_2, and S_3 elements are all zero (see Table 1) and the M_{11} value completely describes the intensity change:

$$S_0' = M_{11}S_0 \tag{10}$$

However, if the incoming light is polarized, then M_{11} is only "one piece of the puzzle" and must be considered in the full equation for the outgoing intensity:

$$S_0' = M_{11}S_0\,(1 + m_{12}s_1 + m_{13}s_2 + m_{14}s_3) \tag{11}$$

Here, M_{11} adjusts the outgoing intensity based on the amount of unpolarized light in the incoming light beam, but the entire first row of the MM may also influence the outgoing intensity for a polarized input light beam.

$$\begin{bmatrix} S_0' \\ S_1' \\ S_2' \\ S_3' \end{bmatrix}_{out} = M_{11} \begin{bmatrix} 1 & m_{12} & m_{13} & m_{14} \\ m_{21} & m_{22} & m_{23} & m_{24} \\ m_{31} & m_{32} & m_{33} & m_{34} \\ m_{41} & m_{42} & m_{43} & m_{44} \end{bmatrix} \cdot \begin{bmatrix} S_0 \\ S_1 \\ S_2 \\ S_3 \end{bmatrix}_{in}$$

Figure 6: MM divided into sections for light attenuation (gray), diattenuation (red), polarizance (blue), and retardance (yellow).

The diattenuation section (red) consists of m_{12}, m_{13}, and m_{14} from the first row of the MM. Attenuation describes the reduction of light intensity, whereas diattenuation describes the preferential reduction of one polarization relative to its orthogonal counterpart. As shown in Figure 7, m_{12} describes the diattenuation between horizontal (x) and vertical (y) linear polarizations; m_{13} describes the diattenuation between +45° and −45° oriented linear polarizations, and m_{14} describes the diattenuation between right (R) and left (L) circular polarizations. When the diattenuation section is combined with the M_{11} value, we can completely describe the outgoing intensity for any incoming light (Eq. (11)).

The polarizance section (blue) consists of m_{21}, m_{31}, and m_{41} from the first column of the MM. These elements describe the ability of the sample to polarize the unpolarized portion of the incoming light beam, as shown in Figure 8. If the sum of the square of these three elements is equal to 1, then unpolarized light will become completely polarized.

The retardance section (yellow) consists of the bottom-right nine elements, as shown in Figure 9. They indicate how the "directions" of polarization will be modified upon interaction with the sample. The diagonal elements (m_{22}, m_{33}, and m_{44}) relate the polarization property of incoming light to the same property for outgoing light. If these diagonal elements equal +1, then those polarization states will not be changed by the sample. For example, if $m_{22} = 1$, horizontal (x) and vertical (y) light must stay horizontal and vertical, respectively. The amplitude and phase of horizontal light may still be altered, but horizontal light will

$$\begin{bmatrix} S_0' \\ S_1' \\ S_2' \\ S_3' \end{bmatrix}_{out} = M_{11} \begin{bmatrix} 1 & m_{12} & m_{13} & m_{14} \\ * & * & * & * \\ * & * & * & * \\ * & * & * & * \end{bmatrix} \cdot \begin{bmatrix} S_0 \\ S_1 \\ S_2 \\ S_3 \end{bmatrix}_{in}$$

Figure 7: Diattenuation section of the MM describes how light intensity is affected by the incoming polarization.

$$\begin{bmatrix} S_0' \\ S_1' \\ S_2' \\ S_3' \end{bmatrix} = M_{11} \begin{bmatrix} 1 & * & * & * \\ m_{21} & * & * & * \\ m_{31} & * & * & * \\ m_{41} & * & * & * \end{bmatrix} \begin{bmatrix} 1 \\ 0 \\ 0 \\ 0 \end{bmatrix}$$

Figure 8: Unpolarized light, as described by the incoming Stokes vector, may become polarized by last three elements in the first column of the MM, referred to as the polarizance section. Thus, when the incoming light is unpolarized the outgoing light may be completely polarized, partially polarized, or unpolarized depending entirely on these elements.

$$\begin{bmatrix} S_0' \\ S_1' \\ S_2' \\ S_3' \end{bmatrix}_{out} = M_{11} \begin{bmatrix} 1 & m_{12} & m_{13} & m_{14} \\ m_{21} & m_{22} & m_{23} & m_{24} \\ m_{31} & m_{32} & m_{33} & m_{34} \\ m_{41} & m_{42} & m_{43} & m_{44} \end{bmatrix} \cdot \begin{bmatrix} S_0 \\ S_1 \\ S_2 \\ S_3 \end{bmatrix}_{in}$$

Figure 9: Retardance section of the MM is shown in yellow. The diagonal elements are highlighted as they describe the outgoing Stokes parameter to the same corresponding Stokes parameter for incoming light.

remain horizontal. If $m_{44} = 1$, *right* and *left* circular light will remain *right* and *left* circular, respectively. At the opposite limit, when a diagonal element is equal to −1 the corresponding polarization states are completely converted to their orthogonal counterparts. If a diagonal element is ±1, the remaining MM elements in the same row and column of the retardance section will be zero because all the incoming light of that type is already described by the diagonal element.

When the diagonal elements are not equal to ±1, the outgoing polarization might be converted ("cross-polarization") between the referenced directions. This "cross-polarization" is further described by the off-diagonal elements in the same row and column of the retardance section. These elements can also be non-zero and will describe entirely what happens to the incoming polarization. This is often best understood by considering the equations that involve the retardance section:

$$S_1' = M_{11}\,(m_{21}S_0 + m_{22}S_1 + m_{23}S_2 + m_{24}S_3) \quad (12a)$$

$$S_2' = M_{11}\,(m_{31}S_0 + m_{32}S_1 + m_{33}S_2 + m_{34}S_3) \quad (12b)$$

$$S_3' = M_{11}\,(m_{41}S_0 + m_{42}S_1 + m_{43}S_2 + m_{44}S_3) \quad (12c)$$

These equations combine with Eq. (11) to completely describe the transformation from incoming to outgoing light properties. Whereas Eq. (11) described the outgoing intensity, Eqs. (12a–c) describe the polarization properties. Each row of the retardance section is related to a specific outgoing polarization property. Each column of the retardance section is related to a specific incoming polarization property. For example, the three elements m_{22}, m_{23}, and m_{24} combine to describe the resulting x-y orientation of the outgoing polarization for any incoming polarized light (with m_{21} describing the effects on unpolarized incoming light).

An MM describing the case where the polarization is not modified may look different for transmission and reflection experiments due to our choice of conventions. The transmitted normalized MM demonstrating no change in polarization is:

$$\begin{bmatrix} 1 & 0 & 0 & 0 \\ 0 & 1 & 0 & 0 \\ 0 & 0 & 1 & 0 \\ 0 & 0 & 0 & 1 \end{bmatrix} \quad (13)$$

We would expect to see such result when measuring transmitted MMSE at normal incidence (0° angle of incidence) through isotropic media. However, the normalized MM for a sample that does not change the polarization state of light in reflection is written as:

$$\begin{bmatrix} 1 & 0 & 0 & 0 \\ 0 & 1 & 0 & 0 \\ 0 & 0 & -1 & 0 \\ 0 & 0 & 0 & -1 \end{bmatrix} \quad (14)$$

This appears to convert ±45° polarizations and *right*/*left* polarizations into their opposite counterparts, as we described in discussion of the retardance section. However, the actual polarization is not modified. This is purely a mathematical necessity due to our choice of convention. Consider Figure 2 for more detail regarding the positive *p*- and *s*- polarization directions for incoming and reflected light. When the light beams move to normal incidence, the electric field for the incoming *p*-polarization opposes the reflected *p*-polarization direction. Thus, the negative m_{33} and m_{44} values are simply there to account for our choice of coordinate system. The transmitted beam shares the same orientation for *p*- and *s*- polarized light as the incoming beam.

There are many samples that will produce the MM values shown in Eqs. (13) and (14) at normal incidence. This will be true for isotropic substrates such as glass or silicon. It will also be true for coated substrates, provided all the materials are isotropic. Thus, a high-low optical stack that produces a very interesting bandpass filter for intensity may produce such an uninteresting MM if all the materials are isotropic, which is often the case for high and low index dielectric layers. In these cases, the only optical response of the sample is an attenuation of light, thus the response is shown solely by the M_{11} value.

Let us consider a few different sample types that populate certain elements of the MM. The MM for an ideal transmitting polarizer aligned with the *x*-axis is shown in Figure 10. A polarizer is a diattenuator, with light along one direction completely attenuated, while the orthogonal direction is transmitted without any attenuation. Here, the prefactor of ½ is shown to explain that the transmitted intensity of unpolarized light will be reduced by half.

All light transmitted through this polarizer will be polarized along the *x*-direction. If the incoming polarization state is *x*-polarized (see Table 1), then all the light intensity will be transmitted through the polarizer:

$$\frac{1}{2}\begin{bmatrix} 1 & 1 & 0 & 0 \\ 1 & 1 & 0 & 0 \\ 0 & 0 & 0 & 0 \\ 0 & 0 & 0 & 0 \end{bmatrix}$$

Figure 10: MM for an ideal polarizer aligned with the *x*-axis.

$$\mathbf{S}' = \frac{1}{2}\begin{bmatrix} 1 & 1 & 0 & 0 \\ 1 & 1 & 0 & 0 \\ 0 & 0 & 0 & 0 \\ 0 & 0 & 0 & 0 \end{bmatrix}\mathbf{S}, \text{ with } \mathbf{S} = S_0\begin{bmatrix} 1 \\ 1 \\ 0 \\ 0 \end{bmatrix} \quad (15a)$$

$$S_0' = \frac{1}{2}S_0 + \frac{1}{2}S_0 = S_0 \quad (15b)$$

If this linear polarizer is rotated to polarize all light along the *y*-axis, then $m_{21} = m_{12} = -1$ and the outgoing intensity for incoming x-polarized light would be zero.

Figure 11 shows the MM for an ideal transmitting retarder, with fast axis aligned along the *x*-axis. This retarder will shift the phase of the *x*-polarization relative to the *y*-polarization by an amount, δ, referred to as the retardance:

Notice in Figure 11 that $m_{22} = 1$ which means the *x*- and *y*- polarized electric fields will remain *x*- and *y*- polarized, respectively. However, their relative phase is shifted, which causes the polarization changes for incoming light that consists of both *x* and *y* polarizations (such as +45°).

We can apply a transformation, as shown in Figure 12, to rotate any MM counterclockwise by an angle ϕ with respect to the original coordinate system:

We can use the expression shown in Figure 12 to also show the MM for a rotated optical element such as a diattenuator or retarder by first rotating from the original coordinate system to match the coordinate system of the

$$\begin{bmatrix} 1 & 0 & 0 & 0 \\ 0 & 1 & 0 & 0 \\ 0 & 0 & \cos\delta & \sin\delta \\ 0 & 0 & -\sin\delta & \cos\delta \end{bmatrix}$$

Figure 11: MM for an ideal retarder aligned along the *x*-axis.

$$\mathbf{R}(\phi) = \begin{bmatrix} 1 & 0 & 0 & 0 \\ 0 & \cos 2\phi & \sin 2\phi & 0 \\ 0 & -\sin 2\phi & \cos 2\phi & 0 \\ 0 & 0 & 0 & 1 \end{bmatrix}$$

Figure 12: MM for a counterclockwise rotation by angle ϕ with respect to an original coordinate system.

rotated optic and then rotating back to the original coordinate system. This will appear as:

$$\mathbf{M}_{\text{rotated}} = \mathbf{R}(-\phi)\mathbf{M}\mathbf{R}(\phi) \tag{16}$$

The more general shapes of a rotated diattenuator or rotated retarder are shown in Figure 13. It can be helpful to watch for these regions of the MM to determine whether a measurement exhibits linear diattenuation or linear retardance and whether the primary polarization effects are along the x, y direction or rotated as shown.

Using Eq. (16), we can show the MM for a rotated ideal polarizer or rotated ideal retarder. The ideal polarizer rotated counterclockwise from our measurement reference frame by an angle ϕ becomes:

$$\frac{1}{2}\begin{bmatrix} 1 & \cos(2\phi) & \sin(2\phi) & 0 \\ \cos(2\phi) & \cos^2(2\phi) & \cos(2\phi)\sin(2\phi) & 0 \\ \sin(2\phi) & \cos(2\phi)\sin(2\phi) & \sin^2(2\phi) & 0 \\ 0 & 0 & 0 & 0 \end{bmatrix} \tag{17}$$

while the ideal retarder rotated counterclockwise from our measurement frame by an angle ϕ becomes:

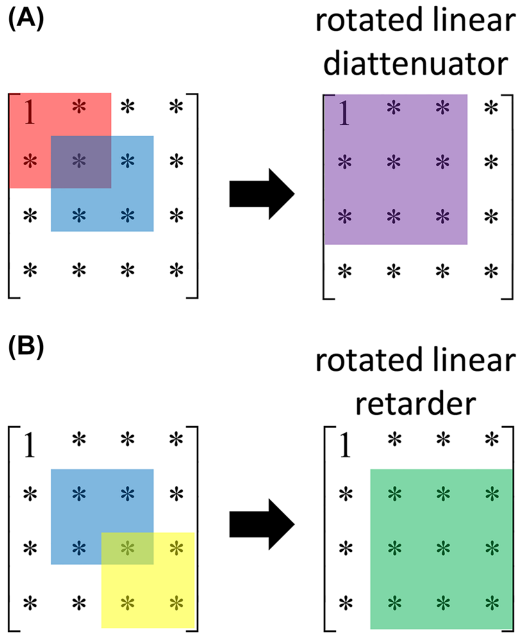

Figure 13: Demonstration of the MM elements that are populated when common optical elements are rotated.
(A) When a linear diattenuator (red) oriented along x/y axes is rotated about the z-axis (shown by the blue rotational "box") it to moves the MM content for the rotated diattenuation into the upper-left nine elements (purple). (B) When a linear retarder (yellow) oriented along the x/y axes is rotated about the z-axis (shown by the blue rotational "box") it moves the MM content for the rotated retarder into the lower-right nine elements (green).

$$\begin{bmatrix} 1 & 0 & 0 & 0 \\ 0 & \cos(\delta)\sin^2(2\phi)+\cos^2(2\phi) & (1-\cos(\delta))\cos(2\phi)\sin(2\phi) & -\sin(\delta)\sin(2\phi) \\ 0 & (1-\cos(\delta))\cos(2\phi)\sin(2\phi) & \cos(\delta)\cos^2(2\phi)+\sin^2(2\phi) & \sin(\delta)\cos(2\phi) \\ 0 & \sin(\delta)\sin(2\phi) & -\sin(\delta)\cos(2\phi) & \cos(\delta) \end{bmatrix} \tag{18}$$

It is interesting to note that m_{44} is independent of the retarder orientation. Thus, δ can be extracted directly from a transmitted MM measurement regardless of sample rotation.

4 Measuring the MM

Instruments that measure the Mueller matrix use optical elements to produce polarized light to probe the sample of interest in what is referred to as the polarization state generator (PSG). After interacting with the sample, the light is analyzed with another set of optical elements, referred to as the polarization state analyzer (PSA), to determine the altered polarization state. The PSG must be capable of producing multiple different polarizations to "fill-in" the various MM elements. Similarly, the PSA must also be capable of varying such that the detected intensity is related to different polarization properties of the light beam (after interaction with the sample). The combination of multiple input states and multiple detected states allows the MM elements to be measured.

An MM ellipsometer continuously modulates a set of optical elements and the detected information is a modulated signal. A Fourier analysis of this signal allows extraction of the MM of any unknown sample. Since ratios of Fourier components are considered, the absolute intensity of the probing and detected light beam is irrelevant for measurement accuracy. In other words, relative polarization changes are detected rather than absolute intensities as would be the case in a reflectometer or polarimeter. This allows MM ellipsometry measurements on samples which scatter part of the light, warped samples, or samples smaller than the probe beam diameter.

Not all ellipsometers, polarimeters, or MMSE instruments measure the complete MM. As we have seen, there is plenty of duplicate information in the common MM shapes from simple samples. The types of optical elements used in such devices will determine which of the MM elements can be measured. The most common optical element is a linear polarizer, which can populate (or analyze) the s_1 and s_2 elements of the Stokes vector depending on the orientation, ϕ, of the polarizer relative to the sample measurement "frame of reference":

$$\begin{bmatrix} 1 \\ \cos(2\phi) \\ \sin(2\phi) \\ 0 \end{bmatrix} \quad (19)$$

A fixed polarizer would only produce or detect one type of polarization. However, rotating the polarizer changes the relative intensity in the s_1 and s_2 elements and allows many measurements. In fact, this over-determines the specific MM elements of interest. In this manner, a simple rotating polarizer allows measurement of the top-left nine elements of the MM, as shown in Figure 14A for rotating polarizer ellipsometer or rotating analyzer ellipsometer configurations. The polarizer does not produce circularly polarized light – always with $s_3 = 0$, so an instrument using only polarizers in the PSG/PSA lacks the ability to measure the last row or last column of the MM.

To measure the last row or column, a compensator can be added to the PSG or PSA. A compensator shifts the phase of one electric field relative to its orthogonal electric field, potentially populating the s_3 Stokes vector. Again, rotation of the compensator allows many different s_3 values to be produced in the probe light and many different s_3 values to be analyzed. Thus, a rotating compensator ellipsometer is often used to determine additional properties of the MM. As shown in Figure 14B and C, a rotating compensator before the sample provides access to the first three rows of the MM, whereas a rotating compensator placed after the sample can measure the first three columns of the MM. If rotating compensators are placed both before and after the sample, as shown in Figure 14D, the complete MM can be measured. The interested reader is directed to reference [77] for a thorough discussion of instrumentation.

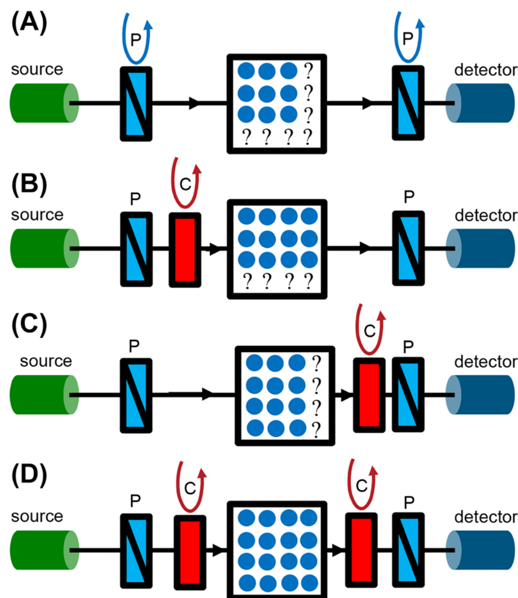

Figure 14: A few common ellipsometry configurations and the corresponding MM elements they can access.
(A) Rotating analyzer and rotating polarizer ellipsometers are prevented from determining the last row and last column of the MM but can measure the upper-left nine elements. Rotating compensator ellipsometers can measure (B) the first three rows or (C) the first three columns of the MM, depending on whether the rotating compensator is before or after the sample, respectively. (D) If rotating compensators are before and after the sample, the entire MM can be measured.

5 Mueller matrix sample properties

5.1 Optical properties

To understand how a sample will influence the polarization of light, we need to consider the optical properties of a material. Optical properties are described by either the complex refractive index ($\tilde{n}$) or complex dielectric function ($\tilde{\epsilon}$), which we define using the "Nebraska conventions" [65]:

$$\tilde{n} = n - ik \quad (20)$$

$$\tilde{\epsilon} = \epsilon_1 - i\epsilon_2 \quad (21)$$

$$\tilde{\epsilon} = \tilde{n}^2 \quad (22)$$

The complex refractive index consists of the index of refraction (or simply index), n, and the extinction coefficient, k. The index describes the phase velocity of light within a material. The extinction coefficient describes the absorption of light, with the following relation to the optical absorption coefficient, α, at wavelength, λ:

$$\alpha = \frac{4\pi k}{\lambda} \quad (23)$$

Together, n and k can describe how light is reflected, transmitted, and absorbed by a material. Using the optical properties of each material, we can describe the overall optical response from multilayers or three-dimensional features.

An isotropic material will have the same optical properties in all directions. Anisotropic materials can have different optical properties for different directions, and as such are described by a dielectric tensor. The optical properties describe how the electric field of light is affected. Thus, anisotropic optical properties describe the polarization direction that will be affected. A linearly anisotropic material may have different optical properties for x-polarized and y-polarized electric fields. Circularly anisotropic materials would differentiate between *right* and *left* polarized electric fields.

The distribution of atoms, molecules, or material structure gives rise to the optical properties of a material. When these properties are direction-dependent and constrained over a large volume, anisotropy may occur. Figure 15 depicts an anisotropic material using different spring tensions in orthogonal directions to describe how the material will respond differently to electric fields depending on orientation relative to the polarization direction.

Optical anisotropy comes in different forms. If there are two uniquely defined optical properties, the material is uniaxially anisotropic. Materials with three uniquely defined optical properties are biaxially anisotropic. Both uniaxial and biaxial anisotropies can be further divided based on whether their anisotropic planes are orthogonal. For simplicity, we will only consider uniaxial and biaxial anisotropy where the anisotropic symmetry planes are orthogonal. Each can be rotated to match the *x*-*y*-*z* coordinate system (where *z* points into the sample perpendicular to the surface), using a sequence of coordinate system rotations called the Euler angles as shown in Figure 16. The Euler angle transformation is used to match the sample axes to the measurement coordinate system. The dielectric tensor of a uniaxial material is written as:

$$\begin{bmatrix} \tilde{\varepsilon}_x & 0 & 0 \\ 0 & \tilde{\varepsilon}_x & 0 \\ 0 & 0 & \tilde{\varepsilon}_z \end{bmatrix} = \begin{bmatrix} \tilde{\varepsilon}_o & 0 & 0 \\ 0 & \tilde{\varepsilon}_o & 0 \\ 0 & 0 & \tilde{\varepsilon}_e \end{bmatrix}, \tag{24}$$

where the two orthogonal directions with the same optical properties are referred to as ordinary (designated with “o”) and the remaining direction with different optical properties is referred to as extraordinary (designated with “e”). The dielectric tensor for a biaxial material is written as:

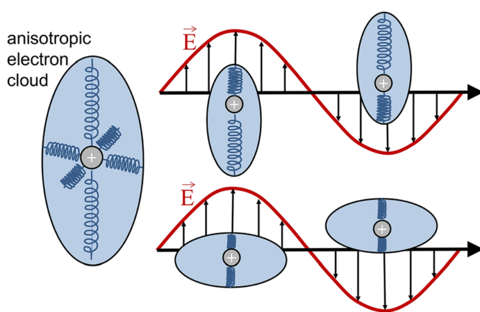

Figure 15: Depiction of anisotropic material, where the optical properties are analogous to springs with different tension along orthogonal axes. The interaction between the anisotropic material and incident light depends on the polarization (direction of the electric field vibration) relative to the material orientation.

$$\begin{bmatrix} \tilde{\varepsilon}_x & 0 & 0 \\ 0 & \tilde{\varepsilon}_y & 0 \\ 0 & 0 & \tilde{\varepsilon}_z \end{bmatrix} \tag{25}$$

Materials with directional-dependent index are referred to as birefringent. Because the index is related to phase velocity of light in a material, birefringence (Δn) can produce a phase difference between orthogonal light waves traveling through the material, often referred to as the retardance. In Figure 17 there are two polarized light waves traveling in the same direction (parallel to the *z*-axis). The left electric field is polarized along the *x*-axis and is subject to n_x. The electric field on the right is polarized along the *y*-axis and is subject to n_y. Assuming the frequency of both electric fields is the same, then $n_x < n_y$ and the *x*-axis is the so-called fast axis. The retardance between *x*- and *y*-axes is measured as the total phase difference between these directions and is dependent on both the birefringence and the path-length. Retardance will appear in the bottom-right nine elements of the MM, as shown in Figure 13B, depending on the orientation of the axes relative to the measurement coordinates.

When the extinction coefficient (absorption coefficient) is direction-dependent, the material is referred to as dichroic. Dichroism will produce diattenuation of light traveling through such material, with the resulting effect shown in the MM depending on the orientation of the dichroism relative to the measurement coordinate system. The total diattenuation will also be path-length dependent.

5.2 MM for isotropic samples

With this basic introduction to optical properties, we turn our attention to how light may interact with a sample – primarily reflection, transmission, or absorption. We start with the most common example encountered in ellipsometry – the reflection of light from an isotropic sample. The sample can consist of a substrate or the substrate can be coated with thin films. The substrate and thin films can be transparent or absorbing. Regardless, if all the materials in the sample are isotropic, the *p*- and *s*- polarizations will be eigenmodes. In other words, these two polarization directions will remain the same upon reflection (or transmission) from the isotropic surface/films. The *p*-polarized incident light will remain *p*-polarized upon reflection or transmission and the same will hold for *s*-polarized light. This may not be true for incoming light of other polarization states. For example, an incident light beam polarized at +45° will most generally convert to elliptically polarized

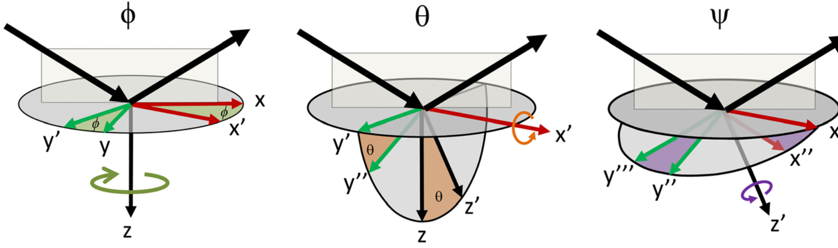

Figure 16: Three Euler angles are a sequence of transformations to match the sample coordinate system to the measurement frame of reference. The choice shown is one of 12 possible sequences, so caution should be used to correctly apply the order and direction of each rotation. Here, the first angle ϕ is a rotation of the *x* and *y* axes around the z-direction, which is pointing into the sample surface. The second angle θ is a rotation of the new y direction, y′, and z directions around the new x direction, x′. The final angle ψ is a rotation of the y′ and x′ directions around z′. All rotations follow the right-hand rule with thumb pointed along the rotation axis.

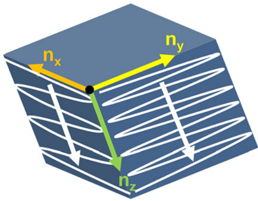

Figure 17: Two electric fields traveling in the same direction experience different refractive indices in an anisotropic material. Thus, each light wave experiences a different phase velocity.

light upon reflection or transmission (which is where ellipsometry gets its name).

Before proceeding we consider the special case of normal incidence. When the light beam enters an isotropic material at normal incidence, the plane of incidence as well as the *p*- and *s*- orientations are undefined. Thus, at normal incidence the *p*- and *s*- electric fields cannot be differentiated and the incoming polarization state does not convert to a different polarization state. The result at normal incidence can be described by the MM of Eqs. (13) and (14) for transmission and reflection of light, respectively. As discussed, we need to account for a 180° phase shift in reflection due to the change in our frame of reference [81]. The only physical alteration to light at normal incidence will be a reduction of light intensity (attenuation) that will be shown in the M_{11} element.

At oblique angles of incidence, the *p*- and *s*- polarizations will experience different attenuations (diattenuation) and different phase shifts (retardance). The measurement coordinate system is defined such that the *p*- and *s*- polarization directions are the *x*, *y* directions, as described earlier. The MM for reflection from an isotropic sample is written as:

$$\begin{bmatrix} 1 & -N & 0 & 0 \\ -N & 1 & 0 & 0 \\ 0 & 0 & C & S \\ 0 & 0 & -S & C \end{bmatrix}, \tag{26}$$

where *N*, *C*, and *S* are related to our ellipsometry parameters from Eq. (2) as [65]:

$$N = \cos(2\Psi) \tag{27a}$$

$$C = \sin(2\Psi)\cos(\Delta) \tag{27b}$$

$$S = \sin(2\Psi)\sin(\Delta) \tag{27c}$$

For this isotropic case, the *n*, *k* values are the same for all directions, yet the MM shows diattenuation between *p*- and *s*- polarized light. This is due to the difference in reflected (or transmitted) intensity for *p*- and *s*- polarizations as shown in Figure 4. Similarly, the *p*- and *s*- polarizations will each experience a different phase change upon reflection (or transmission) which is described by the Δ parameter for standard SE.

The rotation shown in Figure 13 does not cause any change to isotropic samples in reflection or transmission. The optical properties are the same in all directions, thus rotating the sample does not change the experiment. The new plane of incidence still differentiates between *p*- and *s*-polarized light, which are defined by the measurement coordinate system. Thus, rotating the sample produces the same measurement based on Eq. (26) for any sample orientation. Measurements at multiple sample orientations can be used as a test for some types of anisotropies. When the MMSE data are the same for all sample orientations, we cannot conclude that the sample is isotropic, but we can rule out certain types of samples with “in-plane” anisotropy.

5.3 MM for linearly anisotropic samples

When measuring anisotropic materials, the resulting MM depends on the type of anisotropy and the orientation of the anisotropic axes relative to the measurement coordinate system. If the symmetry axes of the anisotropic material are aligned parallel and perpendicular to the plane of incidence, the MM will take the form of an isotropic sample (Eq. (26)). This is demonstrated in Figure 18, where the sample lines represent the anisotropic alignment direction of the material. Thus, the optical properties will be different for electric fields parallel and perpendicular to these lines. In Figure 18A and C the lines are parallel and perpendicular to the plane of incidence, respectively. In both cases, the measured MM will only contain information in the "block on-diagonal" elements as shown in blue. If the sample is rotated such that the anisotropic symmetry axis is no longer parallel/perpendicular to the plane of incidence, the "in-plane" anisotropy can produce "cross-polarization" and populate the "block off-diagonal" elements of the MM as shown in purple for Figure 18B.

It is often desirable to measure MM in transmission at normal incidence, where isotropic materials will not alter the polarization and the measurement is only affected by the anisotropic materials. Figure 19 shows the transmitted MM measured at normal incidence for an α-quartz crystal. The crystal is transparent at the measured wavelengths, so the only optical effect is linear retardance between the *fast*- and *slow*-axes, producing MM elements in the "rotated retarder" section per Figure 13B. The MMSE data in Figure 19 is sensitive to the in-plane retardance and in-plane orientation. The retardance results from the in-plane birefringence (Δn) and the path-length (d) through the crystal. If the thickness (path-length) of the crystal is known, the measured retardance (δ, in units of degrees, waves, or nm) can be related to the underlying birefringence through:

$$\delta_{\text{deg.}} = \frac{360°}{\lambda_0} d\Delta n \tag{28a}$$

$$\delta_{waves} = \frac{1}{\lambda_0} d\Delta n \tag{28b}$$

$$\delta_{nm} = d_{nm}\Delta n \tag{28c}$$

where λ_0 is the wavelength of light in vacuum. For every peak in the retarder section of the MMSE data of Figure 19, there is 360° retardance. MMSE is only sensitive to the relative retardance over a 360° range, as the absolute phase is not measured. However, certain assumptions can be used to infer the absolute retardance. This works best when the MMSE data are collected over a wide spectral range and the overall retardance "order" (total number of 360° phase shifts) is small. The sample's retardance and fast-axis orientation can be directly extracted from the data with the help of Eq. (18). The resulting retardance for this quartz crystal is shown in Figure 20. The MMSE measurement at normal incidence is insensitive to the value of the refractive index along each direction. For a more complete characterization, the crystal would need to be studied at different angles of incidence, in reflection and transmission, and possibly at different sample orientations.

Figure 21 shows the transmitted MM at normal incidence for a 24 µm thick uniaxially-anisotropic substrate with optic axis (i.e. extraordinary direction) parallel to the sample surface. The data are graphed with measured wavelength along the horizontal axis and sample orientation (rotation about the sample normal) along the vertical axis. The colors correspond to the measured MM element values between ±1. Rotation MMSE data often provides excellent visual hints about the sample's

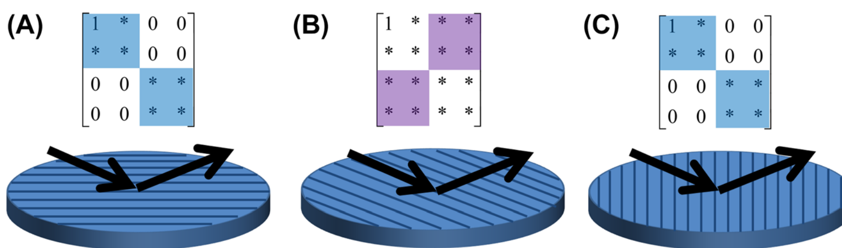

Figure 18: Representation of a sample with in-plane anisotropy. As the sample is rotated about the sample normal, the sample axes change relative to the measurement coordinate system. For sample rotations with anisotropic symmetry axes aligned parallel or perpendicular to the plane of incidence (A, C), the MM measurement will be confined to the "block diagonal" elements shown in blue. Any sample orientation where the anisotropic symmetry axes are rotated between the plane of incidence and its orthogonal direction (B) can produce MM data in the "block off-diagonal" elements shown in purple.

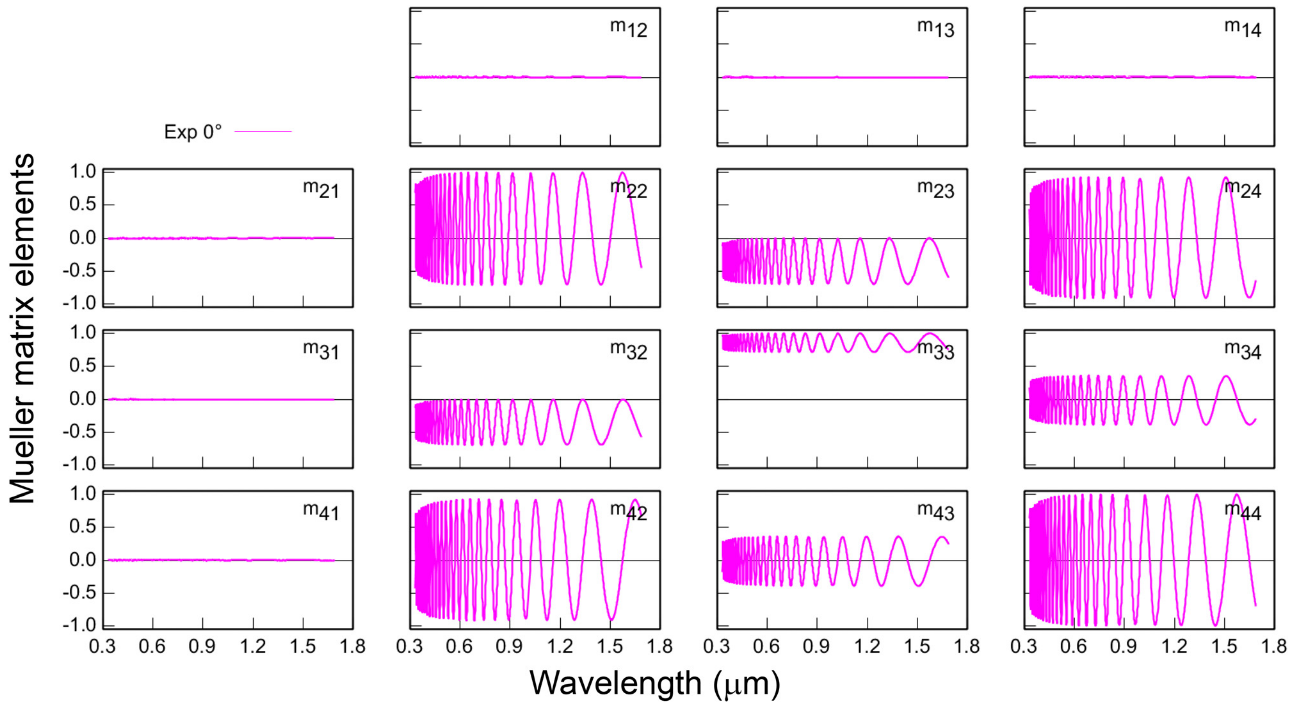

Figure 19: Measurement of transmitted MM at normal incidence through a high-order linear retarder made from α-quartz crystal.

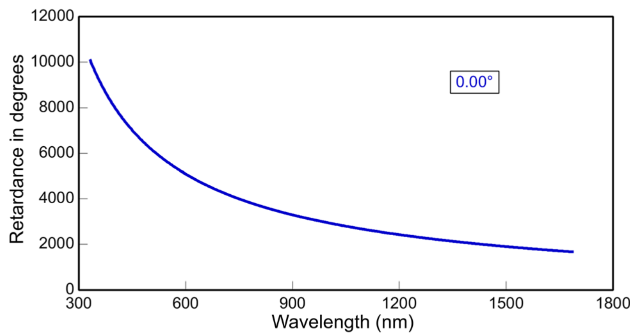

Figure 20: Retardance in degrees for the MM data of the α-quartz crystal shown in Figure 19.

optical symmetry behavior. Whenever the sample's optic axis is aligned parallel or perpendicular to the measurement plane of incidence, the measured MM will be contained within the block-diagonal terms of an unrotated diattenuator or an unrotated retarder (see Figures 10 and 11). The four horizontal dashed lines in Figure 21 were added to show the four azimuthal orientations where the sample and measurement coordinate systems coincide. Given the wide spectral range, we can divide the data into two regions based on observed linear properties. The vertical dashed lines around 900 nm separate these two regions. At wavelengths shorter than 900 nm, the upper left 3×3 block of the MM is active as described in Figure 13A for a rotated linear diattenuator. At wavelengths longer than 900 nm, the lower right $3{\times}3$ block of the MM is active, matching that of a rotated linear retarder per Figure 13B.

These optical phenomena originate from the sample's uniaxial optical properties. MMSE data from multiple angles of incidence and sample orientations enables us to find the direction-dependent complex refractive index. Figure 22 shows the MMSE modeling results, revealing the n_x, n_y, k_x, and k_y of the sample in the measured wavelength range. The sample is transparent for wavelengths above 900 nm and the refractive index in the x-direction is smaller than that in the y-direction. Therefore, the electric field oscillating in the x-direction penetrates faster than the electric field oscillating in the y-direction (linear birefringence), resulting in a phase delay (linear retardance) between the two. While the material is still birefringent at shorter wavelengths, it is also absorbing, and the extinction coefficient of the y-direction is substantially larger than the extinction coefficient of the x-direction. Therefore, most photons associated with the electric field oscillating in the x-direction transmit while the electric field oscillating in the y-direction is absorbed. This explains the linear diattenuation behavior observed in the MMSE data at shorter wavelengths.

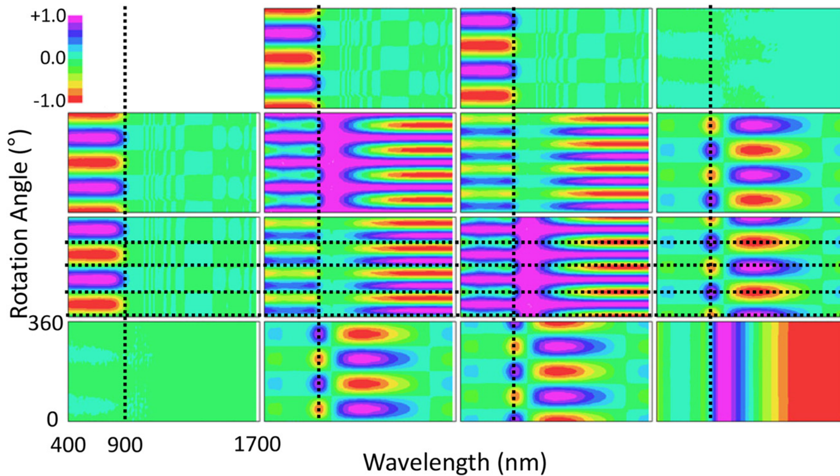

Figure 21: Transmitted MM at normal incidence plotted versus wavelength for a full rotation (sample orientation rotated about the sample normal) of an anisotropic substrate with extraordinary axis parallel to the sample surface. The MMSE data show the linear retardance at longer wavelengths and linear diattenuation at shorter wavelengths.

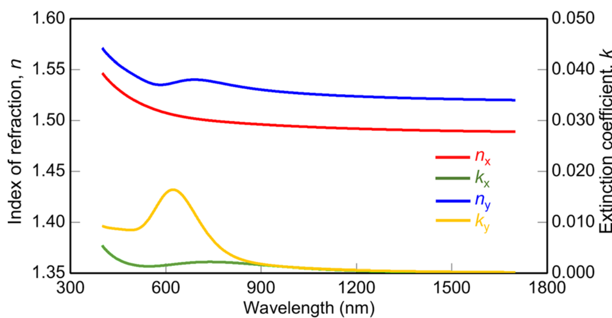

Figure 22: Anisotropic optical constants for the substrate measured in Figure 21.

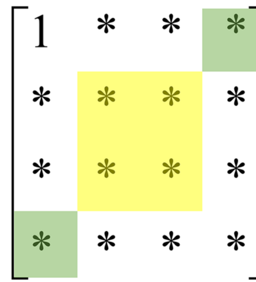

Figure 23: MM sections associated with circular sample properties, including circular diattenuation (green) and circular retardance (yellow).

5.4 MM for circularly anisotropic samples

Samples that differentiate between the circular properties of light include circular diattenuators and circular retarders. The underlying properties that lead to these phenomena are related to different absorptions for *right*-circular light compared to *left*-circular light (circular dichroism) and different refractive indices for *right* and *left* circular polarizations (circular birefringence). The circular polarizing properties of the material can be formed at the molecular level (chiral molecules and certain crystals without mirror symmetry) or at a structural level (helical formation of layers). In either case, the circular optical response is found in the elements of the MM shown in Figure 23.

Here, the green elements show the effects of circular dichroism and the yellow section shows the effects of circular birefringence. In an ideal circular polarizer/retarder, the m_{44} element would be 1.

One common sample that can exhibit circular optical phenomena is a liquid crystal film. Liquid crystal molecules are generally uniaxial and can be arranged to produce both linear and circular optical effects. When the liquid crystal molecules are aligned in a single plane, they can form a linear retarder. However, when liquid crystals arrange in a twisted manner, they can produce circular anisotropic effects. If the twist forms a repeated helical structure, such as in a cholesteric liquid crystal, it can form a Bragg reflector for circularly polarized light. The helical structure will selectively reflect either right or left circularly polarized light and allow the opposite polarization to transmit. The wavelengths affected by such structures depend on the average refractive index for the liquid crystal and the pitch (thickness required for the liquid crystals to twist 360°).

Figure 24 shows the transmitted MM measured at normal incidence for a cholesteric liquid crystal film with nominal 10 μm thickness sandwiched between glass substrates with thin (~30 nm) polyimide alignment layers on each substrate. At normal incidence, the isotropic materials can be ignored as they don't alter the polarization. The liquid crystal is transparent at all measured wavelengths and yet rejects right-circularly polarized light (negative m_{14} forms a left-circular polarizer) in a band around 900 nm wavelength. This is accomplished by the cholesteric liquid

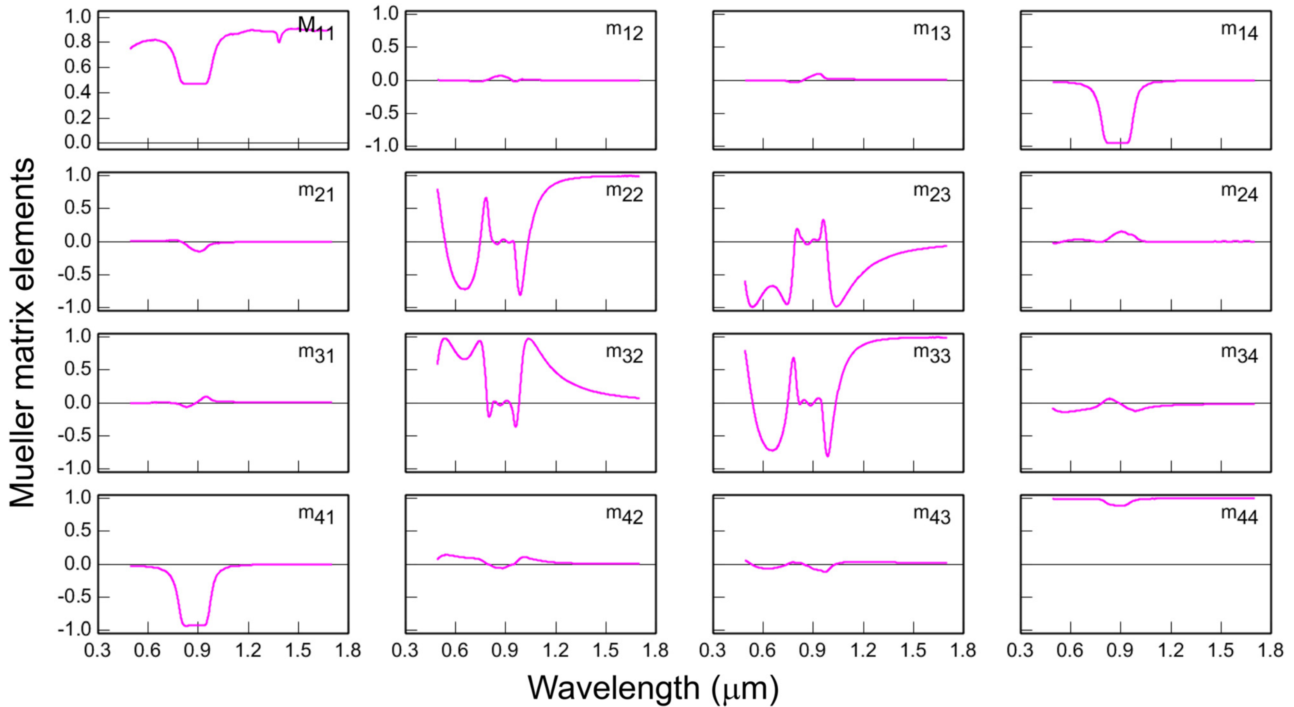

Figure 24: Transmitted MMSE through a cholesteric liquid crystal, 1:1 (Ch-N)GLC, formed between glass substrates. The twisted nature of the liquid crystal produces a circular response as shown in corresponding elements of the MM [82].

crystal orientation turning 18 times between the two substrates. The prominent properties of this MM occur in circular elements shown in Figure 23.

Figure 25 shows the transmitted MMSE data from another sample that produces a circular response. This sample consists of a 90 nm thick achiral polymer film blended with a chiral small-molecule helicene additive (F8T2:aza[M]) on glass substrate [83]. Unlike the cholesteric liquid crystal, which derives its circular optical response from structural rotation of the molecule, the chiral properties in this thin film originate from natural optical activity. A transmission MM ellipsometry measurement alone is not sufficient to distinguish between structural or chiral circular properties, but an additional reflection-type measurement can help to distinguish the two cases [84].

6 Depolarization

A key feature of MM measurements is the ability to describe the depolarizing capability of a sample. A depolarizing sample converts polarized light into partially polarized or unpolarized light, i.e. after interaction with the sample, the phase of the electromagnetic wave varies either spatially, temporally, or spectrally. Thus, the electric field vector is no longer well-defined and can only be described statistically [48]. The Mueller–Stokes formalism can handle depolarizing samples because it represents polarized light in terms of intensities defined as the time-average of different electric field components:

$$I \sim \langle E\,E^{*} \rangle \tag{29}$$

The components of a physical, normalized Stokes vector fulfill the condition [33]:

$$0 \leq \sqrt{s_1^2 + s_2^2 + s_3^2} \leq 1 \tag{30}$$

where the limiting cases of 0 and 1 apply to unpolarized and completely polarized light, respectively. Consequently, the MM for an ideal depolarizer would be given by:

$$\begin{bmatrix} 1 & 0 & 0 & 0 \\ 0 & 0 & 0 & 0 \\ 0 & 0 & 0 & 0 \\ 0 & 0 & 0 & 0 \end{bmatrix} \tag{31}$$

which creates the normalized Stokes vector shown in Table 1 for unpolarized light regardless of the incoming light properties. No real sample shows the ideal shape for the MM in Eq. (31).

In an ideal experiment, all the light within the measurement beam experiences the same sample interaction. In this case, each ray of light witnesses the same MM and

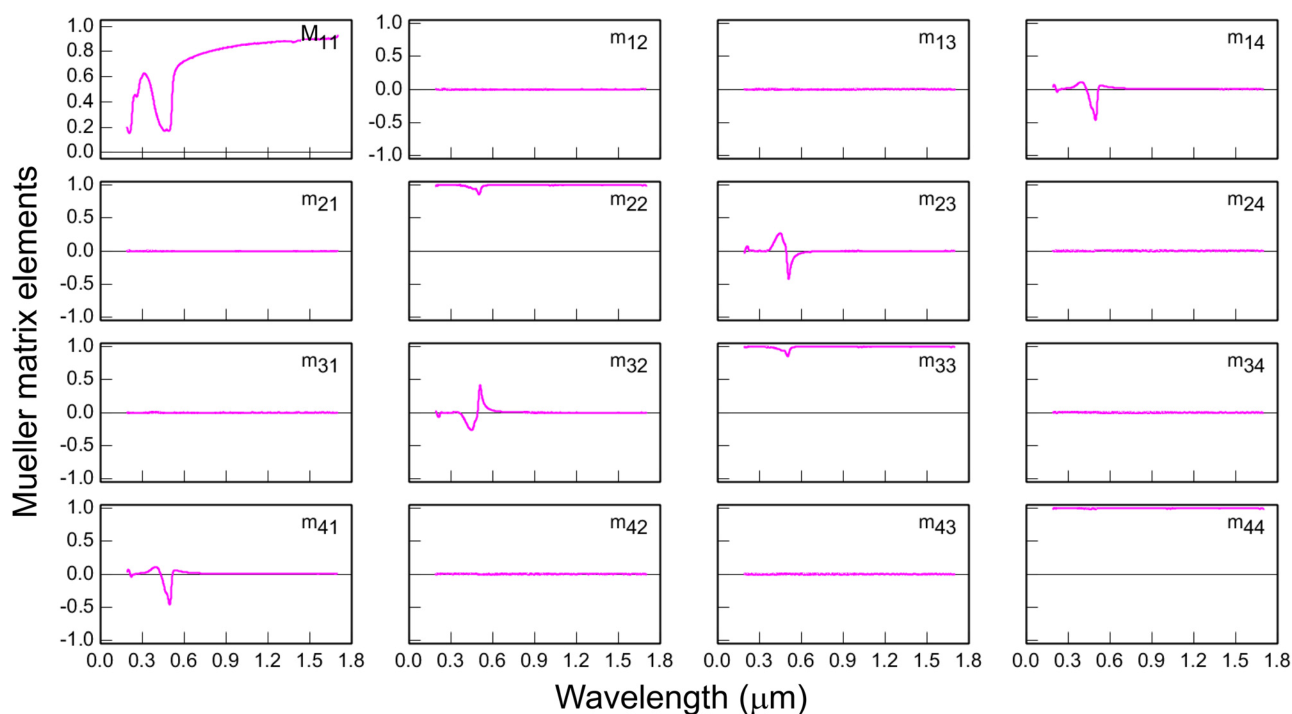

Figure 25: Transmitted MM at normal incidence through a thin achiral polymer film blended with a chiral small-molecule helicene additive (F8T2:aza[M]) [83].

the measured MM is the same as the ideal MM without any loss of polarization ("depolarization"). Depolarization is often the exception, not the rule. Many samples can be measured with negligible depolarization; in which case MMSE measurements are not required (generalized ellipsometry or standard ellipsometry would suffice). However, MMSE measurements allow accurate characterization for any sample, even those that are depolarizing. Thus, we consider the common causes of depolarization. In practice, the loss of polarization is typically associated with the superposition of different beams of light that experience a different interaction with the sample, often described as a "smearing" of polarizations. Superposition can either be coherent, i.e. electric fields sum together as described by the Jones formalism, or incoherent, i.e. intensities sum on the detector as described by the Mueller–Stokes formalism. For the description of depolarization, the incoherent case is more relevant. Two different scenarios occur: spatial incoherence where different light beams are separated laterally to prevent coherent interference and temporal incoherence where the distance traveled by two waves is longer than the coherence length for the specific wavelength.

Some of the most common causes of depolarization in ellipsometry are shown in Figure 26. In each figure, the incident light is represented as linearly polarized. When multiple beams are shown, they are all rays within the same collected measurement beam, used to describe some variable property of the light beam or sample that will be simultaneously measured in the reflected beam. In all cases, the resulting polarization after interacting with the sample is a combination of multiple polarization states and the detector averages over this variety of different beams which are overlapping incoherently. While these figures are all drawn in reflection, the same principles can apply to a transmitted measurement.

Figure 26A represents a non-uniform film thickness. Different portions of the incidence beam interact with different thicknesses, resulting in different reflected polarizations. The thickness variation is within the area of the measurement beam, but spatially separated enough to result in incoherent interference between beams. This thickness variation should not be confused with surface roughness, where the thickness variations occur at a much smaller spatial separation and would not lead to depolarization.

Figure 26B illustrates the effect of a focused measurement – different portions of the measurement beam arrive at different angles of incidence relative to the sample. As such, there can be variation in the measured polarization due to the angular spread of the beams. The measured MM can be considered as coming from the average angle with the depolarization helping to quantify the amount of angular smearing.

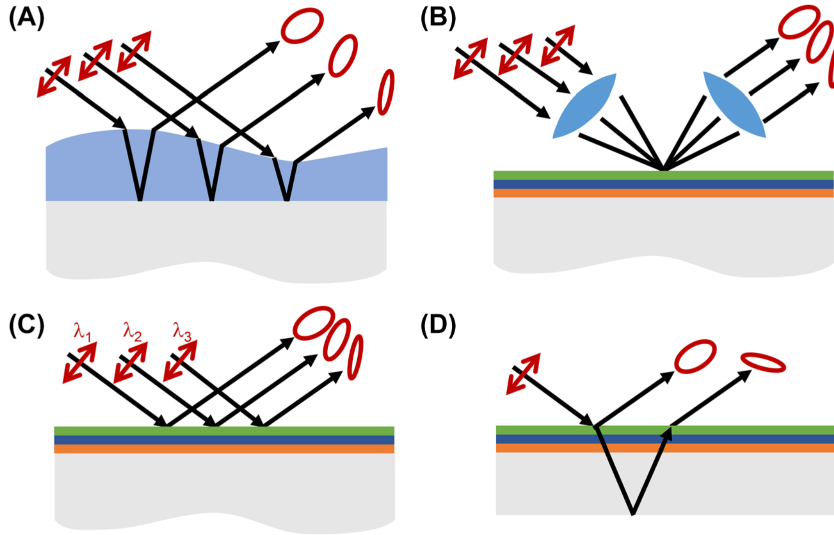

Figure 26: A few common scenarios that may cause depolarization in real samples, including (A) thickness nonuniformity, (B) angular spread, (C) instrument bandwidth, and (D) backside reflections from the substrate. Figure adapted with permission from [65].

Figure 26C illustrates the effect of instrumental bandwidth. Each incoming light beam has a different wavelength. For samples that have a strong specular response, the resulting polarization change for each wavelength can be quite different. If the measurement detects these beams as one, the instrument "bandwidth" may have a significant depolarizing effect.

Finally, Figure 26D shows the light beam reflecting from both front and back surface of a thick substrate. If these two beams are combined at the detector, they can produce depolarization when the reflected beams interfere incoherently. This occurs when the path-length is longer than the coherence length of the beam. For most MMSE measurements at ultraviolet, visible and near infrared light, the substrate becomes incoherent at thickness greater than 50–100 µm. Thus, common glass substrates and semiconductor wafers would produce depolarization when the backside reflections are collected simultaneously with the top-surface reflection.

Of these effects, thickness nonuniformity and backside reflections are sample-related nonidealities, whereas angular spread and wavelength variation (bandwidth) are instrument-related nonidealities.

Most depolarization-causing characteristics can be approximated in a model as a weighted sum of individual MM ($\mathbf{M}_n$) of a varying characteristic such as a layer thickness, and by assuming some weight function (f_n with $\sum f_n = 1$) for each MM:

$$\mathbf{M}_{\mathbf{model}} = f_1\mathbf{M}_\mathbf{1} + f_2\mathbf{M}_\mathbf{2} + \ldots + f_n\mathbf{M}_\mathbf{n} \tag{32}$$

Matching the smeared, generated MM to the measured MM allows extraction of relevant sample properties such as the thickness nonuniformity or the contribution from backside reflections in the measured data. More importantly, the modeling of nonidealities can increase the modeling accuracy for the other sample properties, such as layer thickness and optical constants.

6.1 MM of an isotropic depolarizing sample

For an isotropic, but potentially depolarizing sample, the measured MM would have the following shape:

$$\mathbf{M} = \begin{bmatrix} 1 & -\langle N\rangle & 0 & 0 \\ -\langle N\rangle & 1 & 0 & 0 \\ 0 & 0 & \langle C\rangle & \langle S\rangle \\ 0 & 0 & -\langle S\rangle & \langle C\rangle \end{bmatrix} \tag{33}$$

where the brackets refer to an average of the quantities N, C, and S as detected. For a depolarizing sample, the sum of the squares of these quantities is smaller than 1:

$$\langle N\rangle^2 + \langle C\rangle^2 + \langle S\rangle^2 < 1 \tag{34}$$

The so-called *degree of polarization*, P, is defined as the square root of this relation:

$$P = \sqrt{\langle N\rangle^2 + \langle C\rangle^2 + \langle S\rangle^2} \tag{35}$$

It is common practice to define the quantity:

$$\%Depolarization = \left(1 - P^2\right)100\% \tag{36}$$

where a value of 0% describes a nondepolarizing sample and 100% describes an entirely depolarizing sample. Note that in this definition, the MM element m_{22} remains 1 even in the case of fully depolarized light, which means that individual polarization states retain an isotropic MM, but the superposition of all polarization states smear the information about the sample properties for that wavelength

[16]. Considering the degree of polarization, the measured MM in Eq. (33) can be rewritten as:

$$\mathbf{M} = \begin{bmatrix} 1 & -PN & 0 & 0 \\ -PN & 1 & 0 & 0 \\ 0 & 0 & PC & PS \\ 0 & 0 & -PS & PC \end{bmatrix} \quad (37)$$

The parameters Ψ and Δ reported in commercial analysis software are often derived from the “corrected” form of N, C, and S after the degree of polarization has been separated. Note, that access to at least the fourth row or fourth column of the MM is required to derive P from the measurement data.

6.2 MM of a general depolarizing sample

While the MM is ideally suited for measuring the depolarization of any sample, the depolarization is not simply contained in a single MM element. In the previous example of an isotropic depolarizing sample, we needed to collect MM elements related to N, C, and S to extract the depolarization. A more general MM may contain 15 normalized elements, and each may be affected in some manner by depolarization. Fortunately, there are mathematical calculations to extract information regarding depolarization from the MM. For a general sample, a single quantity, the so-called *depolarization index* (DI) can be defined if the entire 4 × 4 MM is measured [67]:

$$DI = \sqrt{\frac{\left(\sum_{ij} M_{ij}^{2}\right) - M_{11}^{2}}{3M_{11}^{2}}} \quad (38)$$

DI varies between 0 for an ideal depolarizer and 1 for a nondepolarizing sample. If only a partial MM is measured, the so-called *Jones matrix quality factor*, Q_{JM}, can be extracted to indicate if depolarization might be present in the data. This quality factor reports the average difference between the measured partial MM and a best-matching nondepolarizing MM as calculated from a Jones matrix [16].

The primary complaint for any single-valued depolarization figure is their inability to describe the true complexity of the depolarization. The single value assumes the depolarization occurs regardless of input polarization state, while different polarization states may in fact be depolarized by different amounts. Chipman states “Of the 16 degrees of freedom in the Mueller matrix, 1 corresponds to loss, 3 to diattenuation, and 3 to retardance. The remaining 9 degrees of freedom describe depolarization.” [15]. Chipman therefore proposed a surface map of the degree of polarization to represent the dependence on input polarization state similar to a Poincaré Sphere or the average of the degree of depolarization averaged over the entire Poincaré Sphere as a more appropriate measure of depolarization [15]. Again, these quantities require measurement of the entire 4 × 4 MM. Fortunately, the common depolarization encountered during MMSE characterization of thin films and bulk optics are rarely complicated enough to require more than a single-element representation of depolarization.

6.3 Examples of depolarizing MM

In this section, we consider the MM of a few depolarizing samples. Because the depolarization is wrapped within the information throughout the MM, it can be difficult to speculate which MM are depolarizing based on visual appearance. Consider the reflected MMSE data at three angles of incidence for a 5 μm thick film on silicon substrate shown in Figure 27. Based on which MM elements are populated, the thin film is either isotropic or anisotropic with its symmetry axes aligned parallel and perpendicular to the plane of incidence. Because the MM elements are confined to the block-diagonal elements, we can use either Eq. (36) or Eq. (38) to estimate the depolarizing properties of the sample, as shown in Figure 28A and B, respectively. Model calculations matched to the MMSE data show the instrument bandwidth to be approximately 2.6 nm, which is consistent with the CCD detection scheme for the measurement device.

Next, consider MM measurements from a couple anisotropic materials. In Figure 25 we showed the normal-incidence transmitted MMSE data measured through a thin chiral polymer film on glass substrate. Figure 29 shows the reflected MM measurement from a liquid crystal retarder film on glass at 60° angle of incidence. Both measurements show activity in the block off-diagonal MM elements. Visually, it is difficult to ascertain from the MM whether either sample is depolarizing. Because the MM information is not confined to the block-diagonals, the calculation from Eq. (36) would produce erroneous results. Instead, we turn to Eq. (38) to determine whether these samples are depolarizing. The DI for each data set is shown in Figure 30, where only the splayed liquid crystal whose MM is shown in Figure 29 exhibits appreciable depolarization ($DI < 1$).

7 Decomposition methods

There are different approaches to using the measured MM to extract useful information. The simplest is to directly use

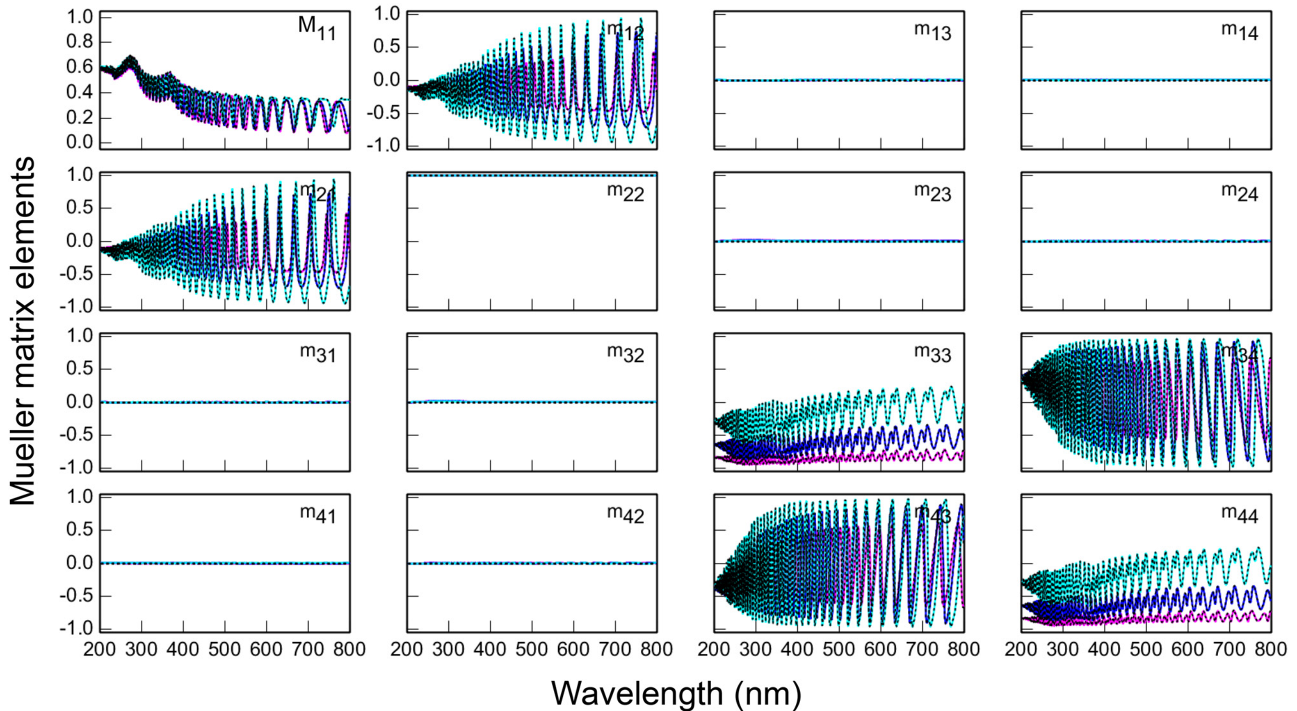

Figure 27: Reflected MMSE measurement from a 5 μm thick, isotropic dielectric film on silicon substrate.

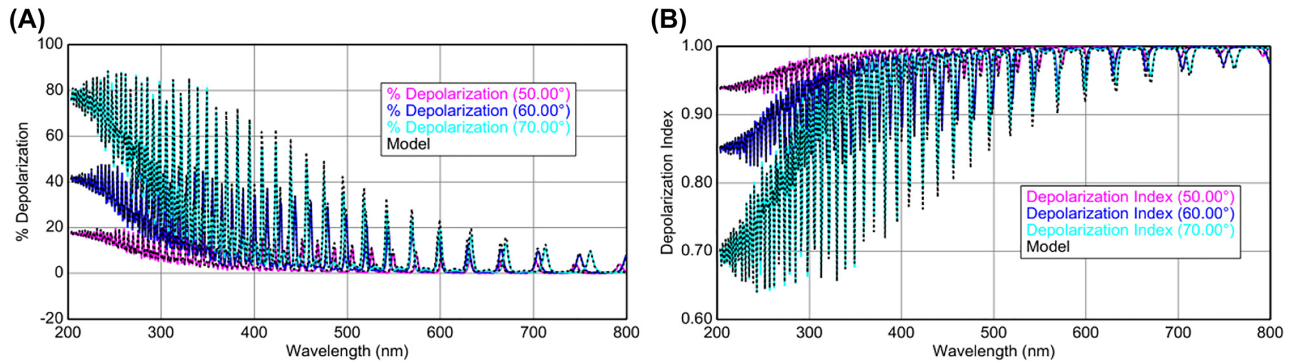

Figure 28: The depolarization from the MMSE measurement in Figure 27 can be calculated using (A) Eq. (33) for percent depolarization or (B) Eq. (38) for depolarization index. The model-fit shown accounts for the finite-bandwidth of the measurement device.

the MM as a transfer function for light interacting with the sample under the same conditions. A more advanced approach is to build a model-based description of the sample to fit the measured data in hopes of extracting the underlying material/sample properties that caused the polarization changes represented in the MM. Such modeling can produce film thicknesses, anisotropic optical properties, and structural properties of a sample, but require significant knowledge and care for all but the simplest samples. Between these two approaches lie the decomposition methods. The goal of applying decomposition to the measured MM is to try to separate it into phenomenological properties.

With the advent of custom-built and commercial instrumentation capable of measuring the entire 4×4 MM, researchers started to explore many phenomena occurring in samples that are far from ideal such as biological or medical specimens. These samples often show large amounts of scattering and depolarization due to spatial inhomogeneity or nonideal structure and are generally difficult, or even impossible, to model [48]. In other situations, researchers might be interested merely in phenomenological quantities describing the nature of a sample, such as linear or circular dichroism in an augmented reality device. In situations like these, MM decomposition methods can be applied to express a complicated experimental MM as a series of

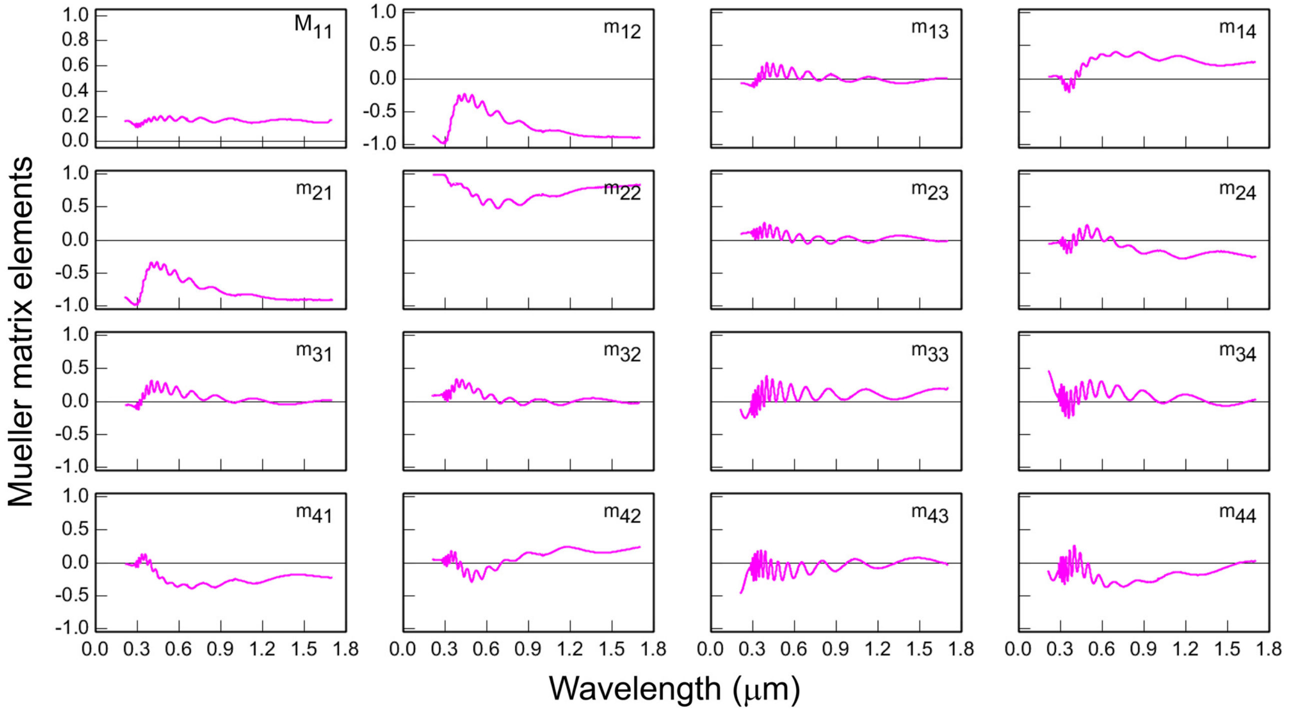

Figure 29: Reflected MM at 60° angle of incidence for a splayed liquid crystal retarder film.

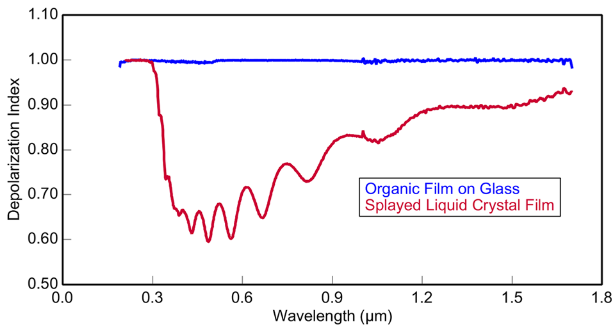

Figure 30: Depolarization index calculated for the MM data of a chiral polymer film (blue, MM from Figure 25) and a splayed liquid crystal retarder (red, MM from Figure 29).

simpler components of well-defined polarization properties, to filter relevant information, or simply to remove noise or depolarization effects from a measured MM. Three major decomposition types are distinguished based on their mathematical characteristics: sum decompositions, product decompositions, and differential decompositions. Each decomposition has its own domain of validity and knowledge of the physical nature of the system studied is required to avoid nonsensical results.

Sum decompositions treat a depolarizing MM as an incoherent addition of nondepolarizing MMs. These decompositions are often applied to test the physical realizability of a measured MM which might not be necessarily satisfied due to experimental error and to potentially filter out the effect of nonidealities. In other cases, individual nondepolarizing MM components might be isolated from a depolarizing MM. The most common sum decomposition was developed by Cloude [12, 68]. This decomposition assumes that any depolarizing MM can be decomposed into a weighted sum of four nondepolarizing MM:

$$\mathbf{M} = \lambda_1\mathbf{M}_1 + \lambda_2\mathbf{M}_2 + \lambda_3\mathbf{M}_3 + \lambda_4\mathbf{M}_4, \tag{39}$$

with positive weight factors. The weight factors are derived as eigenvalues of the so-called covariance matrix [69]. A negative eigenvalue λ_i would indicate a nonphysical MM. By setting negative eigenvalues to zero, nonphysical components such as measurement errors might be filtered out. For more details, the interested reader is referred to the original publications by Cloude [12, 68] and discussions in Ref. [69].

Product decompositions express an arbitrary MM as a product of the elementary MM of a retarder, diattenuator (polarizer), and depolarizer. Different numbers and orders of these matrices are possible, where the order is important because different elementary MM do not commute. These decompositions are particularly useful when a system can *a priori* be described as a sequence of different optical elements. However, different decompositions were developed to cope with more complex situations [69]. The most widely used choice is the Lu–Chipman decomposition [70]:

$$\mathbf{M} = \mathbf{M}_\Delta \mathbf{M}_R \mathbf{M}_D \quad (40)$$

which expresses the MM as a sequential product of submatrices for a diattenuator ($\mathbf{M}_D$), retarder ($\mathbf{M}_R$), and depolarizer ($\mathbf{M}_\Delta$).

A very useful decomposition if phenomenological optical quantities such as linear and circular dichroism or linear and circular birefringence are of interest is the differential decomposition. According to this decomposition, the space derivative along the propagation direction z of an MM can be expressed as [71]:

$$d\mathbf{M}/dz = \mathbf{mM} \quad (41)$$

The 4 × 4 differential matrix $\mathbf{m}$ contains all the elementary properties of the medium, i.e. linear and circular dichroism and birefringence. If the medium can be considered homogeneous along the surface normal over a distance d, the differential matrix can be extracted from:

$$\ln \mathbf{M} = \mathbf{m}d = \mathbf{L} \quad (42)$$

Thus, the term logarithmic decomposition is sometimes used for this decomposition type. For a nondepolarizing sample, we obtain [73]:

$$\mathbf{L} = \begin{bmatrix} 0 & -L_D & -L'_D & C_D \\ -L_D & 0 & C_B & -L'_B \\ -L'_D & -C_B & 0 & L_B \\ C_D & L'_B & -L_B & 0 \end{bmatrix} \quad (43)$$

Here, C_B and C_D refer to circular birefringence and dichroism, L_B and L_D to linear birefringence and dichroism for horizontal and vertical polarization, and L'_B and L'_D to the linear birefringence and dichroism for ±45° reference directions. Note that the definitions of the birefringence terms in Eq. (43) contain the effect of sample thickness and the wavelength, which differs from the common use of the term "birefringence" for the index difference (Δn). The interested reader is referred, for example, to Ref. [70] for clarifications. For a depolarizing MM, sum decomposition can be performed to first extract a nondepolarizing MM. Alternatively, ln $\mathbf{M}$ can be split into one part with the nondepolarizing features and a second part carrying depolarization [66, 74, 75].

We recently used the differential decomposition to extract chiral properties of sugar solutions, alpha-quartz, liquid crystals, beetle cuticle, and cellulose nanocrystal films in comparison with the same quantities as determined by electromagnetic modeling of the actual material properties using the Tellegen constitutive relations [73]. Figure 31 shows the C_B and C_D for a cholesteric glassy liquid crystal sample determined by differential decomposition of

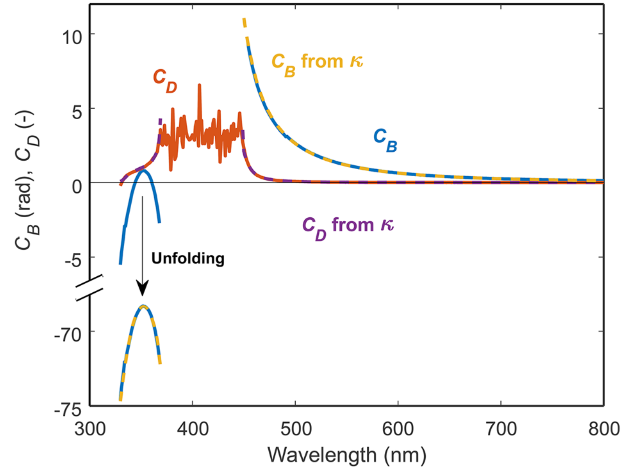

Figure 31: Circular dichroism CD and circular birefringence CB for a cholesteric glassy liquid crystal sample determined by differential decomposition of MM data (solid curves). The dashed curves show CB and CD calculated from electromagnetic modeling of the Tellegen chirality parameter κ. See Ref. [73] for details. Reprinted with permission from [73].

MM data in comparison to the same quantities as determined by electromagnetic modeling of the Tellegen chirality parameter κ.

The reader is guided to Refs. [48, 69, 70] for more detailed discussions, additional decomposition versions, and examples.

8 MMSE applications

The applications of MMSE can be quite complex and the following examples should be considered as demonstrations of what is possible in the field by skilled practitioners. There are many applications in the literature and their review can be better understood with knowledge of the basic concepts provided in earlier sections of this tutorial. For example, a beginner to the field may benefit simply from matching general "shapes" of the various MM data presented to those from Section 3. We start with the MMSE data from a uniaxial MgF_2 crystal, which is used as a retarder in optical experiments. The MMSE measurements can determine the amount of retardance versus wavelength and angle of incidence. Next, we consider the MMSE characterization of flexible plastic substrates at infrared wavelengths where the polymer exhibits many direction-dependent molecular vibrations. The third example covers a nematic liquid crystal where MMSE characterization can determine the amount and direction of twisting in the molecules throughout the layer. Finally, we show

results from MMSE characterization of a "Gate-all-around" or "Nanosheet" FET, the next generation after "FINFET", test structure used to determine the critical dimensions before and after a selective-etch process.

8.1 MgF_2 crystal

MMSE measurements are particularly useful in studying both the optical constants and the resulting optical response from anisotropic crystals. Here, we consider a 1 mm thick disc of MgF_2. The MgF_2 crystal is uniaxial and its optical axis is normal to the polished surfaces. This is confirmed with an MMSE measurement in transmission through the crystal at normal incidence, shown in Figure 32. The MM resembles that shown in Eq. (13), where there is no change in polarization as the light travels parallel to the extraordinary crystal axis and the electric field, which is orthogonal to the direction of beam propagation, only experiences the ordinary refractive index. Considering M_{11}, which remains above 0.9, we know the crystal is transparent over the measured wavelength range, which was from 190 nm in the ultraviolet to 1690 nm in the near infrared.

To introduce retardance, the crystal can be tilted such that the electric field parallel to the tilt direction will experience the projection of the extraordinary axis (and corresponding n_e), while the electric field perpendicular to the tilt direction will only experience n_o. Thus, a tilt of the uniaxial crystal allows controlled retardance between these orthogonal directions. MMSE data in transmission through the MgF_2 crystal is shown in Figure 33 at 0°, 5°, 10°, and 15° angle of incidence. While there is no retardance at normal incidence (0°), the bottom-right 2 × 2 block of the MM exhibits increasing retardance with increasing tilt angle. If our goal is to understand the amount of retardance introduced by the crystal as a function of transmitted angle of incidence, the MMSE can be directly used to extract the retardance for each angle, as shown in Figure 34. This calculation is based on Eq. (18) with no rotation angle, which reduces to the form shown in Figure 11.

Consider the MM shape from Figure 33 in more detail. The interesting elements are confined to the bottom-right 2 × 2 elements – those of an unrotated retarder. The MgF_2 crystal is anisotropic, but we do not witness any cross-polarization that would inform us of this anisotropy. This is explained by Figure 18 – when we tilt the crystal, the anisotropic directions are always aligned with the *p*- and *s*-directions of our measurement setup. Thus, we can have anisotropy without cross-polarization. If we had tilted the crystal in an arbitrary direction, we could have produced an MMSE measurement that would have appeared like that of the rotated retarder from Eq. (18) and shown in Figure 13B.

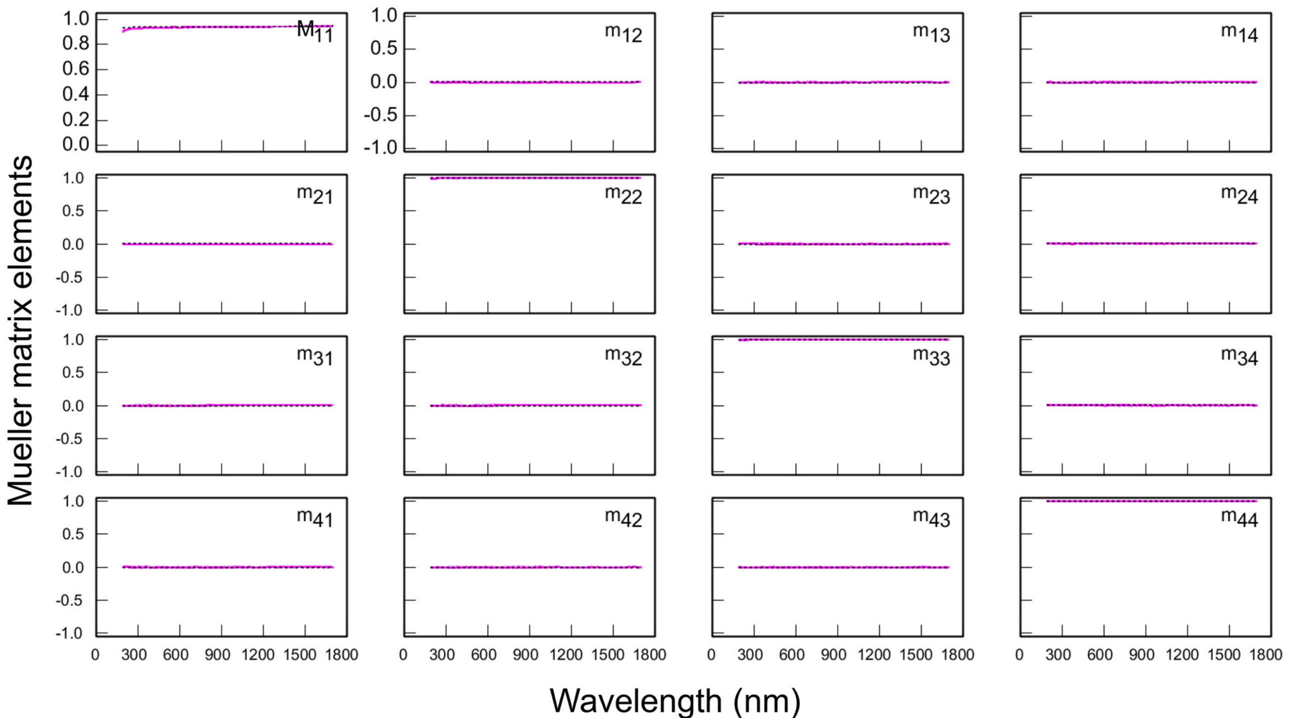

Figure 32: MMSE data transmitted at normal incidence through MgF_2 crystal.

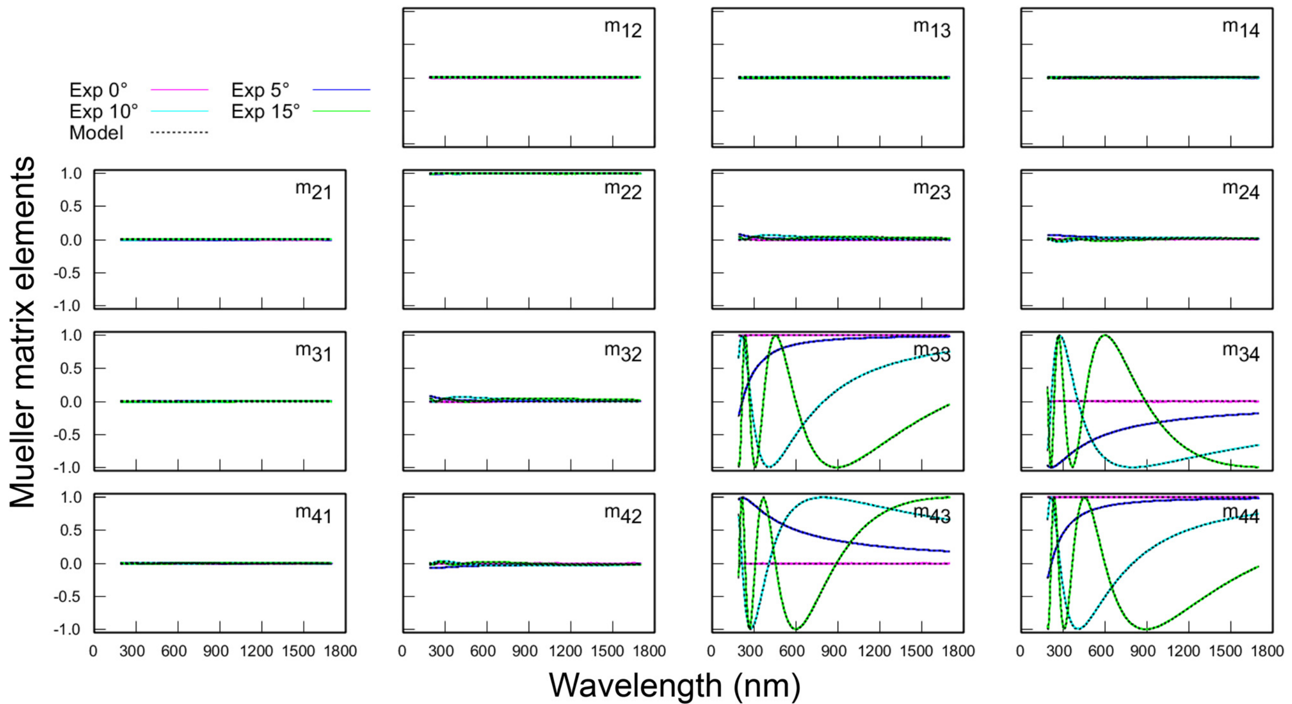

Figure 33: MMSE data in transmission through the MgF_2 crystal at 0°, 5°, 10°, and 15° angles of incidence.

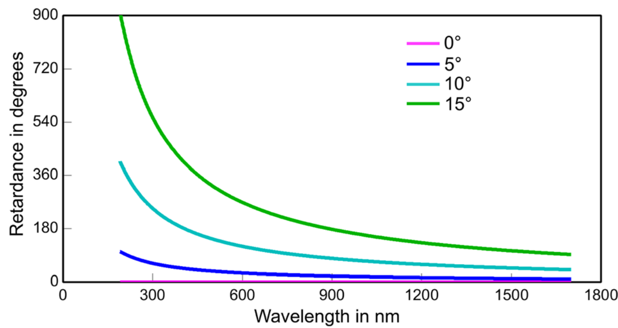

Figure 34: Calculated retardance from the MMSE data of MgF_2 crystal shown in Figure 33.

The MMSE data from a crystal can be used to determine more than just the retardance for light traveling through the crystal at specific wavelengths and angles of incidence. The data can also be used to determine the underlying reason for that retardance – the path length and the birefringence ($\Delta n = n_o - n_e$). For unknown crystals, the thickness can often be approximated by a separate measurement (e.g., digital calipers) to allow model-fitting for the birefringence. Alternately, if the crystal optical constants are well-known, the thickness can be determined from the MMSE data. MMSE data was collected in both transmission and reflection for this crystal at a wide range of angles of incidence. The MMSE data in Figure 35 are transmitted through the crystal from −20° to +70° at every 0.25°. The data curves are shown versus angle of incidence at a wavelength of 301 nm. The data are symmetrical around 0° with only slight activity in the cross-polarization retarder terms (m_{23}, m_{24}, m_{32}, and m_{42}). The cross-polarization is the result of a tilt of only 0.128° between the optical axis and the ellipsometer coordinate system. This tilt is perpendicular to the plane of incidence, which is why the cross-polarization terms appear. If the tilt was in the plane of incidence, the result would be a slight shift in the data symmetry around the 0° measurement angle.

The MMSE data shown in Figure 36 is for the reflected angles from 20° to 70° for the MgF_2 substrate at a wavelength of 632 nm. The detected light is collected from both front and back surfaces of the crystal. Light that travels through the crystal and returns to the surface will experience a phase retardance between *p*- and *s*-polarizations for the same reason we have phase retardance at oblique angles in transmission. The data in both transmission (Figure 35) and reflection (Figure 36) were fit to a model describing the MgF_2 crystal optical constants and thickness. Using published literature values for the MgF_2 optical constants in ordinary and extraordinary direction [85], the total substrate thickness would need to be adjusted to 1.0654 mm which is a 6.54% deviation from the nominal thickness. Alternately, we could fix the thickness at the nominal value and fit for the wavelength-dependent

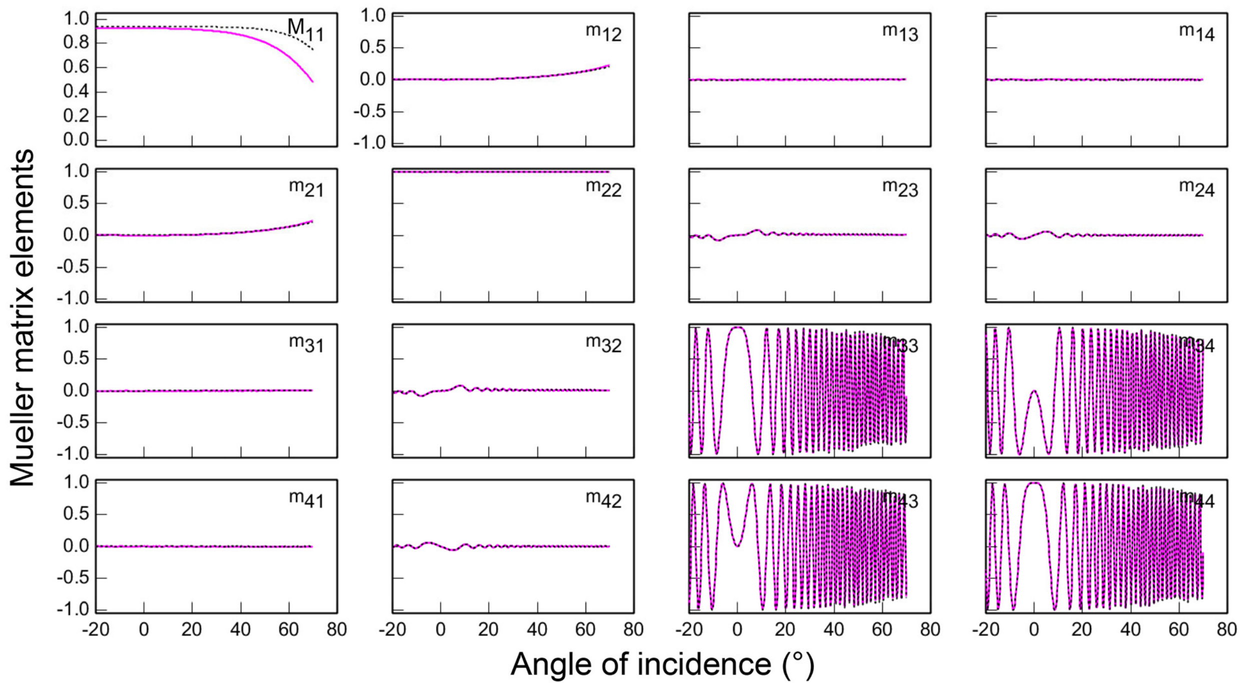

Figure 35: MMSE data and corresponding fit for transmitted measurements through MgF_2 crystal at 301 nm versus angle of incidence.

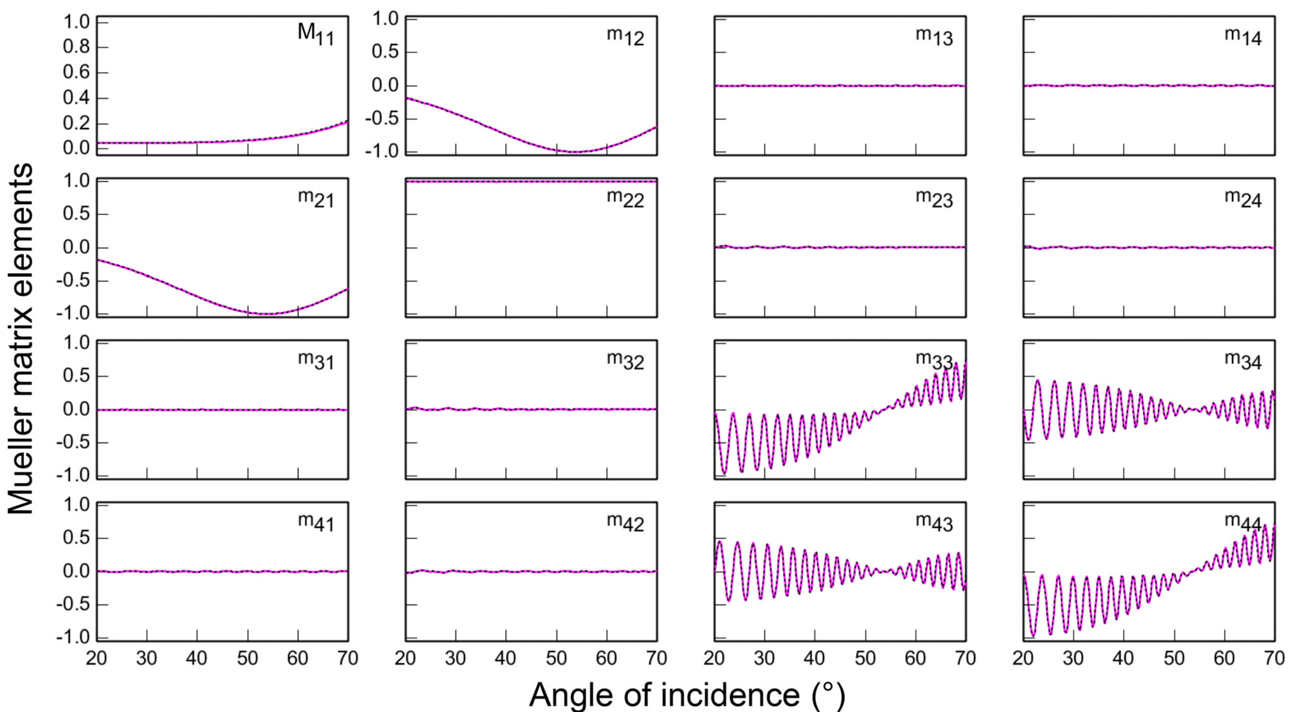

Figure 36: MMSE data and corresponding fit for data reflected from MgF_2 crystal at 632 nm wavelength versus angle of incidence.

birefringence of the MgF_2 crystal. The result would be an index difference at 633 nm of 0.01255 instead of the book-value index difference of 0.01178 – an equivalent 6.54% deviation in birefringence. Here, the MMSE measurement cannot determine which is correct, so we need to turn to other measurements to distinguish the correct modeling approach. A digital caliper reading of the substrate shows a thickness of 1.06 mm, so it appears the reference

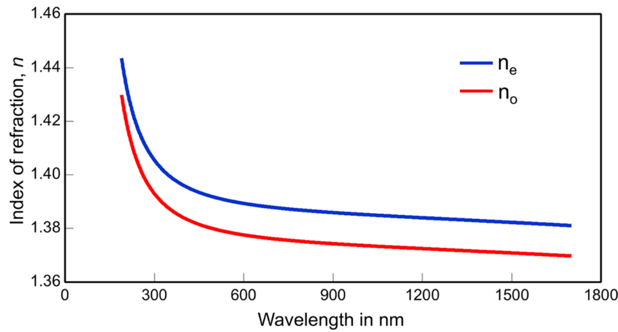

Figure 37: Uniaxial refractive index for MgF_2 crystal, from [85].

values for the ordinary and extraordinary refractive index of MgF_2 (shown in Figure 37) are accurate and we were able to determine the thickness of this substrate. This shows the importance of an accurate thickness when measuring bulk crystals in transmission, which often comes from separate measurements, to extract accurate Δn values from MMSE data.

The reader may recall that one of the benefits of MMSE measurements is the ability to also measure partially polarized light. The transmitted MM measurements remain primarily polarized, except at short wavelengths and large angles of incidence as shown in Figure 38, which shows the depolarization index for both 0° and 65° transmitted data. The depolarization index is also graphed in Figure 38 for 20° and 65° reflected angles. In reflection, the depolarization is much more prominent, especially at smaller angles of incidence. To understand this, we can model (and fit) the various effects that were discussed in Section 6. The model-fitted curves for each data set are also shown in Figure 38. Our transmitted measurements are modeled with only the instrument bandwidth, which is estimated at 2.8 nm. In addition to the instrument bandwidth, the reflected data model needs to include the contribution from light

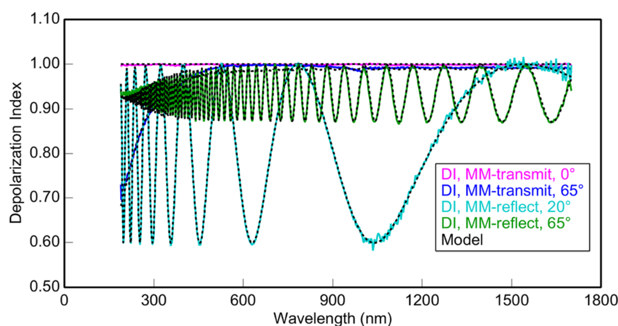

Figure 38: Depolarization index for two MMSE data sets in transmission (0° and 65° angles of incidence) and two in reflection (20° and 65°).

reflecting from the back surface of the substrate and reaching the detector. This light is incoherent with the front-surface reflection, which is why it contributes strongly to the depolarization.

8.2 Flexible plastic substrates

Flexible plastic substrates often show stretch-induced anisotropy due to the preferred orientations of the polymer chains. Typical examples for flexible electronics applications are polyethylene terephthalate (PET), polyethylene naphthalate (PEN), and polyimide sheets, all of which show biaxial anisotropy. These materials are transparent in the visible and near-infrared, so backside-reflected light can have a strong influence on optical measurements. For example, the phase shift between the *p*- and *s*- polarizations traveling through the biaxially anisotropic sheet affect the ellipsometry data. Cross-polarization may occur when the sample's anisotropy coordinate system is not aligned with the ellipsometer coordinate system. As flexible sheets are typically very thin, from a few micrometers to less than a hundred micrometers, reflections from both front- and back-surfaces can even combine coherently. This leads to high-frequency, thickness-related interference patterns in the measured data. In addition, even a small amount of thickness non-uniformity or instrument bandwidth can cause significant depolarization. Therefore, MMSE provides the ideal measurement for a flexible plastic substrate that may exhibit anisotropy, cross-polarization, and depolarization.

To simplify characterization, one could roughen the backside to avoid light collection from this surface and approximate the front surface using the pseudo optical constants from standard SE data [86]. However, we have shown that the "apparent index" of a biaxial substrate obtained from this method is neither the same as any of the true biaxial indices nor consistent when the sample azimuth or angle of incidence is varied [87]. We have demonstrated proper ellipsometry modeling strategies for various plastic sheets with different degrees of birefringence that utilize MMSE data [34]. Data analysis finds the true biaxial optical constants of flexible plastic substrates where $\tilde{n}_x \neq \tilde{n}_y \neq \tilde{n}_z$.

Figure 39 shows the partial MM data of a 50 μm thick PEN substrate mainly in the near-to-mid infrared spectrum (wavelengths from 1 to 14.5 μm). The fourth column of the MM is missing as the infrared ellipsometer used for measurements uses a rotating compensator after the sample per the configuration shown in Figure 14C. The magenta curves represent the MM data at normal incidence in transmission, whereas the blue curves are for an oblique

angle of 55° in reflection. We selected only a few spectra from amongst the plethora of data collected at various angles of incidence and rotational azimuths for illustration. In general, transmission MMSE data helps find the azimuthal angle and linear birefringence of the sample. Before collecting the reflected MMSE data, the back surface of the substrate was roughened to scatter reflections from this surface. However, we still model the sample as a biaxial substrate rather than using the pseudo optical constants approach. The two different blue curves show the MMSE data at two sample orientations rotated by 90°. Notice that the curves in off-diagonal block elements are non-zero, especially in the absorbing region, even though light was only collected from the front surface reflections. According to the ellipsometry modeling results, these two measurements are collected when the sample is oriented at −45° and +45°, respectively. The index of refraction of the biaxially anisotropic PEN substrate is shown in Figure 40, revealing the direction-dependent complex IR absorption features and their Kramers–Kronig consistent counterpart.

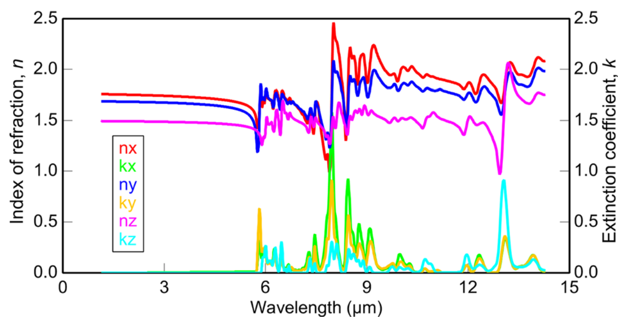

Figure 40: Complex refractive index for biaxially anisotropic PEN substrate.

8.3 Twisted nematic liquid crystal

Liquid crystals are used in many display technologies to manipulate the polarization of light. As such, their polarization-dependent properties are of significant interest. When the liquid crystal molecules are aligned and their

Figure 39: Infrared MMSE data collected in transmission (magenta) and reflection (blue) from a PEN substrate.

movement is confined, they exhibit anisotropic optical properties. The optical response can be used to produce phase retarders and switchable devices. We considered data from a linear retarding crystal of α-quartz in Figure 19. Compare that measurement to MMSE transmitted measurement of a 6.2 μm thick nematic liquid crystal in Figure 41. Both MMSE data sets populate the bottom-right nine elements of the MM, related to their retarding properties. The α-quartz produces a much larger phase shift than the nematic liquid crystal, determined by considering the number of data oscillations versus wavelength from both Figures. However, something more interesting occurs in the MMSE data for the nematic liquid crystal. While it is not easy to visually identify that the retarder in Figure 41 is twisted, the trained user would notice that the amplitudes of the off-diagonal oscillations vary significantly versus wavelength. Compare this to the very regular behavior of the linear retarder data shown in Figure 19 and one can conclude that this sample is "special".

Rotation MMSE data can offer better visual clues of whether the in-plane retarder is "twisted". Consider the transmitted MMSE data for an untwisted linear retarder in Figure 42 versus sample rotation. There are four sample

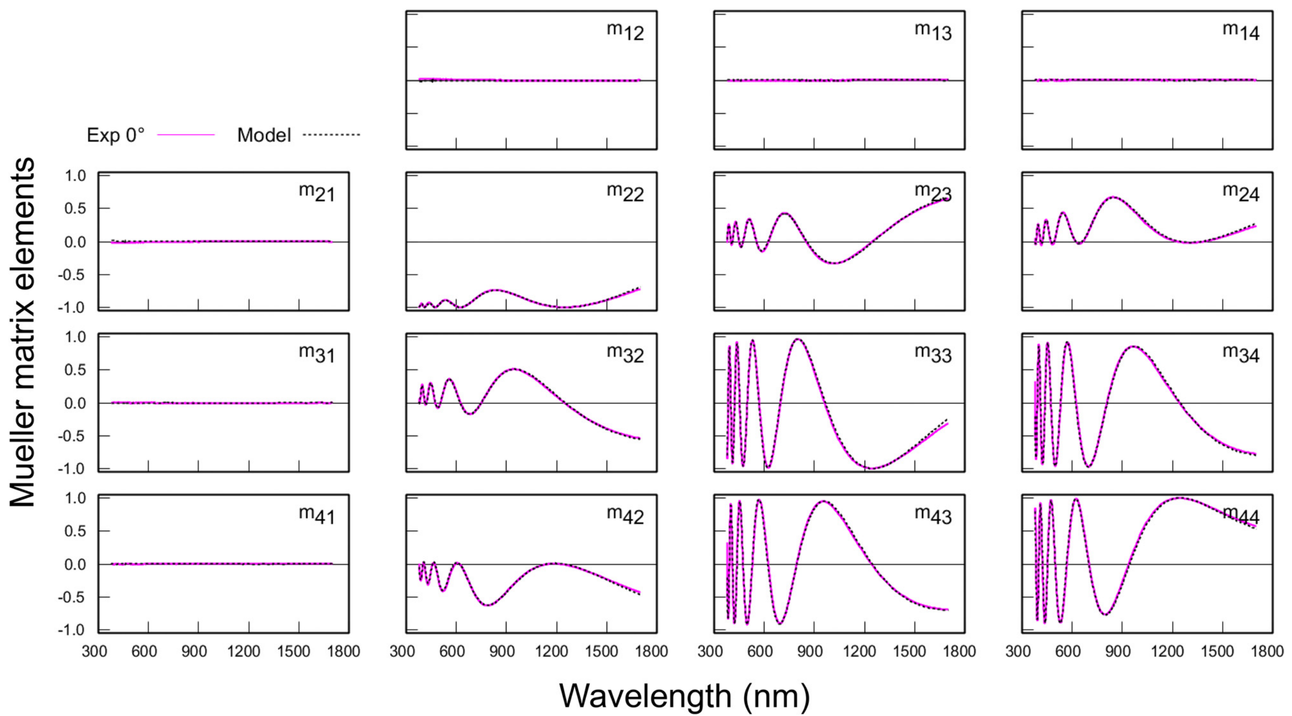

Figure 41: Transmitted MM measurement at normal incidence through a nematic liquid crystal film sandwiched between coated glass slides. The model-fit results are generated from a 6.2 μm anisotropic layer with counterclockwise rotating orientation through the film as looking along the beam-path.

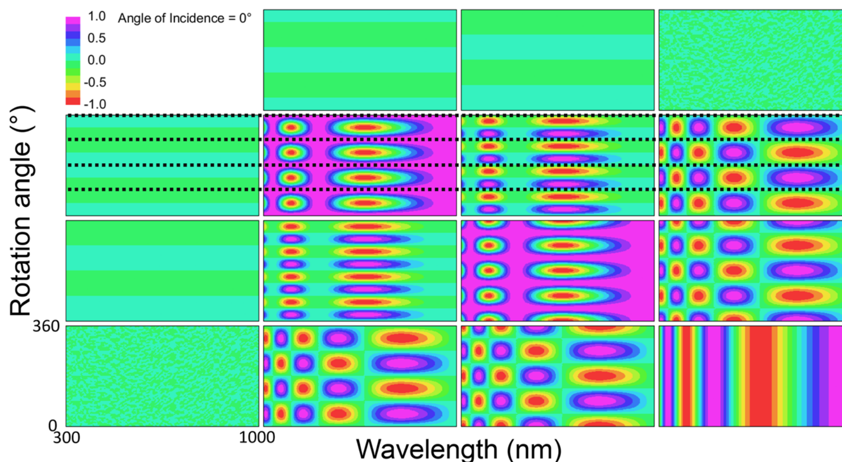

Figure 42: Rotational MMSE data in transmission at normal incidence for a linear retarder.

orientations where the retarder is aligned parallel or perpendicular to the plane of incidence (as designated by the dashed lines). At these four orientations, the block off-diagonal elements are 0 and $m_{22} = 1$ for all wavelengths.

Next, consider the same MMSE transmitted experiment for a twisted anisotropic retarder shown in Figure 43. When the orientation is twisted, we are unable to locate any sample orientations where the block off-diagonal elements equal 0 for all wavelengths. This is most evident when considering the last row and the last column of the MM, which shows the twisting of the MM elements compared to Figure 42. Note that m_{44} is independent of sample orientation for either sample case.

Returning to the MMSE data for our twisted nematic liquid crystal from Figure 41, recall that normal-incidence MMSE data is insensitive to the layer thickness, so this value is fixed at a previously determined value. Modeling the data with uniaxially anisotropic layer results in the refractive indices shown in Figure 44. The liquid crystal orientation (extraordinary direction) is found to be rotated −3.7° relative to the ellipsometer frame of reference at the interface with the glass substrate. The liquid crystal twists counterclockwise as seen looking in the direction of beam travel by a total of 89.6°.

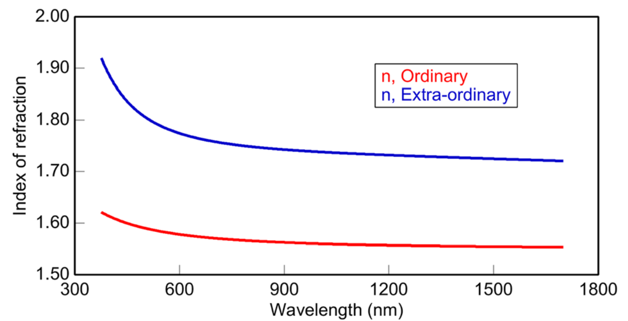

Figure 44: Anisotropic refractive index for a nematic liquid crystal, determined from model-fit to the MM data in Figure 41.

8.4 MMSE in semiconductor metrology

In recent years, MM ellipsometry was established as an industry standard for extremely sensitive, non-destructive metrology of the critical dimensions in semiconductor microelectronic devices. Modern integration paradigms and ever shrinking transistor dimensions led to the formation of periodic, subwavelength size features which act as diffraction gratings. The optical contrast between the materials involved in the process enables the reconstruction of not only the pitch and outer dimensions of these gratings, but also determination of intricate, inner features such as liner and spacer thicknesses, remaining hard mask thicknesses after lithography processes, filling of void spaces, buried layers, etc. [55, 78–80]. The term “optical critical dimension” metrology was established for optical methods capable of measuring these parameters. Advanced modeling algorithms such as RCWA, finite element methods, or finite-difference time-domain are applied for the reconstruction of the dimension information from the raw measurement data. With the transition from planar device geometries to FinFETs and recently to nanosheet transistors, measurement of the relative phase information between *p*- and *s*-polarization contained in the on-diagonal block elements and the access to the cross-polarization terms in the off-diagonal blocks of the MM proved extremely sensitive to slight asymmetries and even allows characterization of the etching behavior during the release of buried nanosheet channels [55, 78–80]. As an example, Figure 45 shows the optical model setup for a test structure intended to demonstrate the sensitivity to individual SiGe sacrificial layer indentations created by variations in this etch process, adapted from Ref. [78].

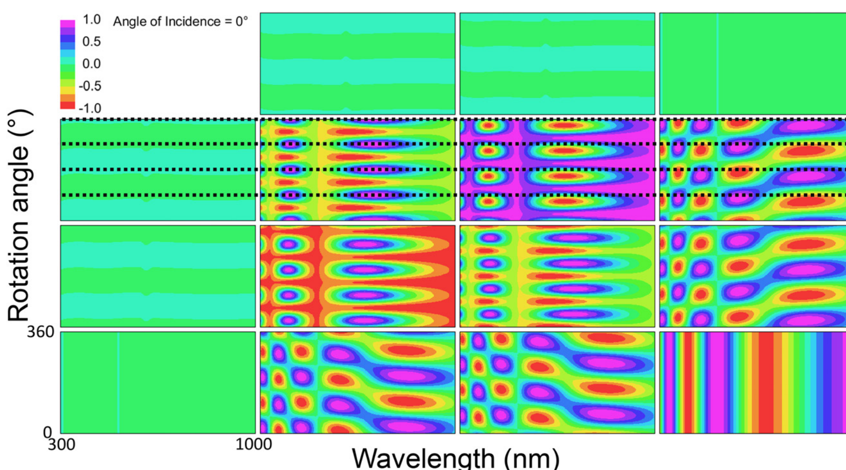

Figure 43: Rotational MMSE data in transmission at normal incidence for a twisted linear retarder.

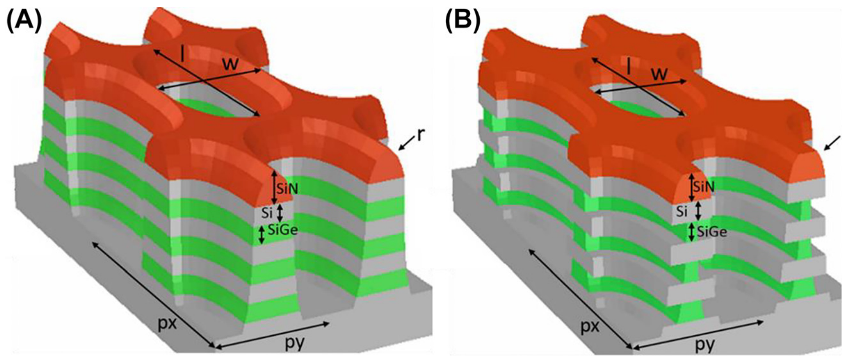

Figure 45: Scatterometry model for (A) unetched nanowire test structure (B) etched nanowire test structure after regression analysis. The parameters floated for analysis for (A) and (B) are: (1) length (l) of hole; (2) width (w) of the hole; (3) thickness values of the Si and SiGe nanosheets, SiN hard mask layer; (4) extent of rounding (r) of the top SiN layer; and (5) pitch in x (px) and y (py) directions. Reproduced from [78], with the permission of AIP Publishing.

The test structures consist of a cross pattern etched by an anisotropic etch step into a layer stack of alternating SiGe and Si nano sheets which emulates the dimensions in a typical fin created during an actual nanosheet transistor device process. In a selective etch step, the sacrificial SiGe sheet width is reduced while the Si nanosheet width is not altered. The parameters of interest for this setup are given in the caption of Figure 45. While only a single test structure is shown, the sample consists of a periodic array of the same structures filling the measurement area. A comparison between experimental MMSE data and the best matching RCWA calculation model for a selectively etched sample with 10.5 nm indent in the SiGe nanosheets is shown in Figure 46. For the etched structures, the amount of SiGe selective cavity etch, side wall angle of the SiGe and the curvature of the SiGe etch were successfully extracted. Close correspondence between values obtained from optical critical dimension analysis with scanning electron microscopy (SEM) and transmission electron microscopy (TEM) imaging analysis emphasized that

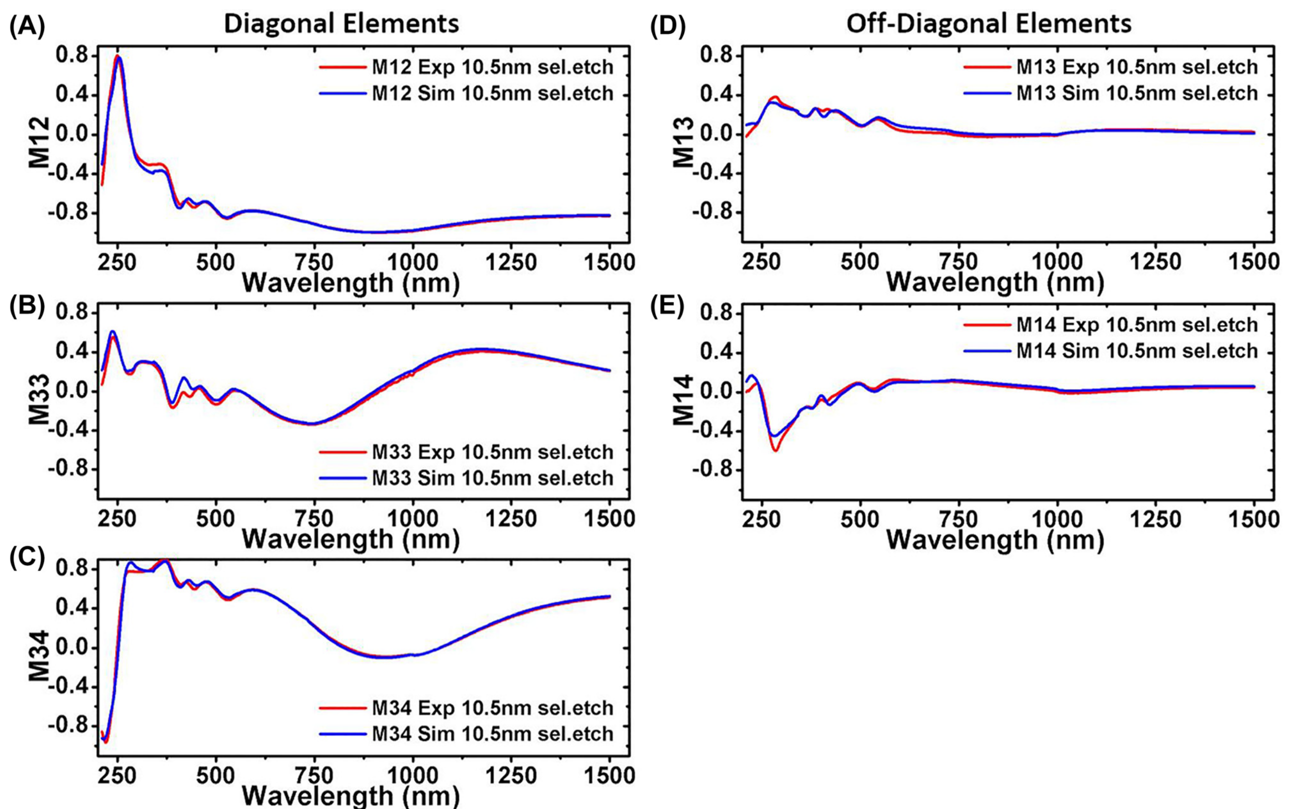

Figure 46: Comparison of experimental and best-matching RCWA model (somewhat misleadingly referred to as "simulated" in Ref. [78]) for m_{12}, m_{34}, m_{33}, m_{13}, m_{14} for a selectively etched sample with 10.5 nm indent, at a nominal azimuthal angle of 45°. Reproduced from [78], with the permission of AIP Publishing.

MMSE-based scatterometry has the capability to extract profile dimensions of complex subsurface features. Please refer to Ref. [78] for further details.

Recently, model-free approaches based on machine learning which compares experimental MMSE data with reference data from alternative slower or destructive metrology techniques such as SEM or TEM gained importance. These approaches do not require manual input, fine tuning of the geometry parameters and inclusion of nonidealities to match the experimental data closely and rather relate minute spectral variations to very real changes in the device structure. It is expected that machine-learning based MMSE scatterometry in combination with further hardware improvements will enable accurate process control well into the future Å-size technology node era.

9 Conclusions

MMSE is increasingly popular as a nondestructive characterization solution for various thin films, nanostructures, metamaterials, and critical dimensions. The Mueller–Stokes calculus builds a theoretical foundation to describe the interaction between polarized light and matter based on measurable light intensities. MMSE provides access to the sample's polarizing, cross-polarizing, and depolarizing properties upon reflection, transmission, and absorption and is thus applicable to any conceivable sample type. The MM of a sample contains information about light attenuation, diattenuation, polarizance, retardance, and depolarization. Knowledge of the MM elements, sections, and common shapes provide a guide to the interpretation of any measurement. The optical response of any sample can be forward calculated by simply multiplying the measured MM with a defined input Stokes vector without the need for a model analysis. Phenomenological quantities of a sample can be extracted from the MM using mathematical equations describing retarders and polarizers, or by applying MM decomposition methods. MMSE modeling based on Fresnel equations or RCWA enables determination of the complex refractive index for isotropic samples, the dielectric function tensor in anisotropic materials, thin-film thickness, underlying material, and structural properties or subwavelength critical dimensions in periodic samples. We have demonstrated the power of MMSE by considering a few case studies such as linear retarders, flexible anisotropic substrates, liquid crystals, very thick films with significant depolarization, and optical critical dimension measurements, to highlight just a few of the many applications of MMSE.

The interested reader is referred to the many excellent publications in this ever-growing field. For basic details regarding ellipsometry, a good place to start are references [65, 76]. MMSE details are also included in reference [65] and a great additional resource is reference [48]. To better understand the Stokes–Mueller mathematics, readers are encouraged to check out references [15, 33, 67]. If you are still excited after these excellent texts, the remaining references can be your guide to additional details.

Acknowledgements: We acknowledge Shaw Chen, Mitchell Anthamatten, Wenshi Zhang, and Mattias Hartveit from the University of Rochester for preparing the cholesteric liquid crystal used for Figure 24.
Author contributions: All the authors have accepted responsibility for the entire content of this submitted manuscript and approved submission.
Research funding: None declared.
Conflict of interest statement: The authors declare no conflicts of interest regarding this article.

References

[1] K. Jarrendahl and B. Kahr, in *Hans Mueller (1900-1965)*, J.A.Woollam Co., Inc. Newsletter, 2011, pp. 8–9.
[2] N. G. Parke, *Matrix Optics*, Ph.D. dissertation, Massachusetts Institute of Technology, Cambridge, Mass., 1948.
[3] N. G. Parke, “Optical algebra,” *J. Math. Phys.*, vol. 28, p. 131, 1949.
[4] G. G. Stokes, “On the composition and resolution of streams of polarized light from different sources,” *Trans. Cambridge Phil. Soc.*, vol. 9, p. 399, 1852.
[5] C. Brosseau, “Polarization and coherence optics: historical perspective, status, and future directions,” in *Progress in Optics*, E. Wolf, Ed., Amsterdam, London, New York, Elsevier, 2009, pp. 149–208.
[6] P. Soleillet, “Sur les paramètres caractérisant la polarisation partielle de la lumière dans les phénomènes de fluorescence,” *Ann. Phys.*, vol. 12, p. 23, 1929.
[7] F. Perrin, “Theory of light scattering by macroscopically isotropic bodies,” *J. Chem. Phys.*, vol. 10, p. 415, 1942.
[8] R. C. Jones, “A new calculus for the treatment of optical systems, I. Description and discussion of the calculus,” *J. Opt. Soc. Am.*, vol. 31, no. 7, p. 488, 1941.
[9] E. S. Fry and G. W. Kattawar, “Relationships between elements of the Stokes matrix,” *Appl. Opt.*, vol. 20, p. 2811, 1981.
[10] J. J. Gil and E. Bernabeu, “A depolarization criterion in Mueller matrices,” *Opt. Acta*, vol. 32, p. 259, 1985.
[11] R. Simon, “Mueller matrices and depolarization criteria,” *J. Mod. Opt.*, vol. 34, p. 569, 1987.
[12] S. R. Cloude, “Conditions for the physical realisability of matrix operators in polarimetry,” *Proc. SPIE*, vol. 1166, p. 177, 1989.

[13] J. J. Gil and E. Bernabeu, “Depolarization and polarization indices of an optical system,” *Opt. Acta*, vol. 33, p. 185, 1986.
[14] R. A. Chipman, “Depolarization index and the average degree of polarization,” *Appl. Opt.*, vol. 44, p. 2490, 2005.
[15] R. A. Chipman, W. S. T. Lam, and G. Young, *Polarized Light and Optical Systems*, USA, CRC Press, 2018.
[16] J. N. Hilfiker, J. S. Hale, C. M. Herzinger, et al., “Estimating depolarization with the Jones matrix quality factor,” *Appl. Surf. Sci.*, vol. 421, p. 494, 2017.
[17] R. M. A. Azzam, “Photopolarimetric measurement of the Mueller matrix by Fourier analysis of a single detected signal,” *Opt. Lett.*, vol. 2, p. 148, 1978.
[18] D. H. Goldstein, “Mueller matrix dual-rotating retarder polarimeter,” *Appl. Opt.*, vol. 31, p. 6676, 1992.
[19] O. Arteaga, J. Freudenthal, B. Wang, et al., “Mueller matrix polarimetry with four photoelastic modulators: theory and calibration,” *Appl. Opt.*, vol. 51, p. 6805, 2012.
[20] P. S. Hauge, “Mueller matrix ellipsometry with imperfect compensators,” *J. Opt. Soc. Am.*, vol. 68, p. 1519, 1978.
[21] R. M. A. Azzam, “Mueller-matrix ellipsometry: a review,” *Proc. SPIE*, vol. 3121, p. 396, 1997.
[22] R. W. Collins and J. Koh, “Dual rotating-compensator multichannel ellipsometer: instrument design for real-time Mueller matrix spectroscopy of surfaces and films,” *J. Opt. Soc. Am. A*, vol. 16, p. 1997, 1999.
[23] J. Lee, J. Koh, and R. W. Collins, “Dual rotating-compensator multichannel ellipsometer: instrument development for high-speed Mueller matrix spectroscopy of surfaces and thin films,” *Rev. Sci. Instrum.*, vol. 72, p. 1742, 2001.
[24] A. Furchner, C. Kratz, W. Ogieglo, et al., “Ultrasensitive broadband infrared 4×4 Mueller-matrix ellipsometry for studies of depolarizing and anisotropic thin films,” *J. Vac. Sci. Technol. B*, vol. 38, p. 014003, 2020.
[25] J. L. Pezzaniti and R. A. Chipman, “Mueller matrix imaging polarimetry,” *Opt. Eng.*, vol. 34, p. 1558, 1995.
[26] J. M. Bueno and M. C. W. Campbell, “Confocal scanning laser ophthalmoscopy improvement by use of Mueller-matrix polarimetry,” *Opt. Lett.*, vol. 27, p. 830, 2002.
[27] O. Arteaga, M. Baldrís, J. Antó, et al., “Mueller matrix microscope with a dual continuous rotating compensator setup and digital demodulation,” *Appl. Opt.*, vol. 53, p. 2236, 2014.
[28] J. Chang, H. He, Y. Wang, et al., “Division of focal plane polarimeter-based 3×4 Mueller matrix microscope: a potential tool for quick diagnosis of human carcinoma tissues,” *J. Biomed. Opt.*, vol. 21, no. 5, p. 056002, 2016.
[29] C. Y. Han, C. Y. Du, and J. Y. Jhou, “Rapid full Mueller matrix imaging polarimetry based on the hybrid phase modulation technique,” *Opt Commun.*, vol. 382, p. 501, 2017.
[30] J. Angelo, T. Germer, and M. Litorja, “Structured illumination Mueller matrix imaging,” *Biomed. Opt Express*, vol. 10, p. 2861, 2019.
[31] S. Funke, M. Duwe, F. Balzer, et al., “Determining the dielectric tensor of microtextured organic thin films by imaging Mueller matrix ellipsometry,” *J. Phys. Chem. Lett.*, vol. 12, p. 3053, 2021.
[32] R. M. A. Azzam and N. M. Bashara, *Ellipsometry and Polarized Light*, The Netherlands, North Holland, 1986.
[33] D. H. Goldstein, *Polarized Light*, 3rd ed. USA, CRC Press, 2011.
[34] N. Hong, R. A. Synowicki, and J. N. Hilfiker, “Mueller matrix characterization of flexible plastic substrates,” *Appl. Surf. Sci.*, vol. 421, p. 518, 2017.
[35] N. Hong and J. N. Hilfiker, “Mueller matrix ellipsometry study of a circular polarizing filter,” *J. Vac. Sci. Technol. B*, vol. 38, p. 014012, 2020.
[36] I. Dahl, “How to measure the Mueller matrix of liquid-crystal cells,” *Meas. Sci. Technol.*, vol. 12, p. 1938, 2001.
[37] S. T. Tang and H. S. Kwok, “Mueller calculus and perfect polarization conversion modes in liquid crystal displays,” *J. Appl. Phys.*, vol. 89, p. 5288, 2001.
[38] J. N. Hilfiker, B. Johs, C. M. Herzinger, et al., “Mueller-matrix characterization of liquid crystals,” *Thin Solid Films*, vol. 455, p. 591, 2004.
[39] J. N. Hilfiker, B. Johs, C. M. Herzinger, et al., “Generalized spectroscopic ellipsometry and Mueller-matrix study of twisted nematic and super twisted nematic liquid crystals,” *Thin Solid Films*, vol. 455, p. 596, 2004.
[40] N. J. Podraza, C. Chen, I. An, et al., “Analysis of the optical properties and structure of sculptured thin films from spectroscopic Mueller matrix ellipsometry,” *Thin Solid Films*, vol. 455, p. 571, 2004.
[41] L. M. S. Aas, M. Kildemo, Y. Cohin, et al., “Determination of small tilt angles of short GaSb nanopillars using UV-visible Mueller matrix ellipsometry,” *Thin Solid Films*, vol. 541, p. 97, 2013.
[42] R. Magnusson, J. Birch, P. Sandström, et al., “Optical Mueller matrix modeling of chiral $Al_xIn_{1-x}N$ nanospirals,” *Thin Solid Films*, vol. 571, p. 447, 2014.
[43] D. Schmidt, B. Booso, T. Hofmann, et al., “Monoclinic optical constants, birefringence, and dichroism of slanted titanium nanocolumns determined by generalized ellipsometry,” *Appl. Phys. Lett.*, vol. 94, p. 011814, 2009.
[44] T. Hofmann, D. Schmidt, A. Boosalis, et al., “THz dielectric anisotropy of metal slanted columnar thin films,” *Appl. Phys. Lett.*, vol. 99, p. 081903, 2011.
[45] D. Schmidt and M. Schubert, “Anisotropic Bruggeman effective medium approaches for slanted columnar thin films,” *J. Appl. Phys.*, vol. 114, p. 083510, 2013.
[46] C. Rice, A. Mock, D. Sekora, et al., “Control of slanting angle, porosity, and anisotropic optical constants of slanted columnar thin films via in situ nucleation layer tailoring,” *Appl. Surf. Sci.*, vol. 421, p. 766, 2017.
[47] U. Kılıç, A. Mock, R. Feder, et al., “Tunable plasmonic resonances in Si-Au slanted columnar heterostructure thin films,” *Sci. Rep.*, vol. 9, p. 71, 2019.
[48] M. Losurdo, and K. Hingerl, Eds. *Ellipsometry at the Nanoscale*, Germany, Springer, 2013.
[49] G. E. Jellison, Jr, M. A. McGuire, L. A. Boatner, et al., “Spectroscopic dielectric tensor of monoclinic crystals: $CdWO_4$,” *Phys. Rev. B*, vol. 84, p. 195439, 2011.
[50] C. Sturm, R. Schmidt-Grund, C. Kranert, et al., “Dipole analysis of the dielectric function of color dispersive materials: application to monoclinic Ga_2O_3,” *Phys. Rev. B*, vol. 94, p. 035148, 2016.
[51] A. Mock, R. Korlacki, S. Knight, et al., “Anisotropy, phonon modes, and lattice anharmonicity from dielectric function tensor analysis of monoclinic cadmium tungstate,” *Phys. Rev. B*, vol. 95, p. 165202, 2017.
[52] A. Mock, R. Korlacki, C. Briley, et al., “Band-to-band transitions, selection rules, effective mass, and excitonic contributions in monoclinic $\beta{-}Ga_2O_3$,” *Phys. Rev. B*, vol. 96, p. 245205, 2017.

[53] A. Mock, R. Korlacki, S. Knight, et al., "Anisotropy and phonon modes from analysis of the dielectric function tensor and the inverse dielectric function tensor of monoclinic yttrium orthosilicate," *Phys. Rev. B*, vol. 97, p. 165203, 2018.
[54] C. Sturm, S. Höfer, K. Hingerl, et al., "Dielectric function decomposition by dipole interaction distribution: application to triclinic $K_2Cr_2O_7$," *New J. Phys.*, vol. 22, p. 073041, 2020.
[55] J. Li, J. J. Hwu, Y. Liu, et al., "Mueller matrix measurement of asymmetric gratings," *J. Nanolithogr. MEMS, MOEMS*, vol. 9, p. 041305, 2010.
[56] M. Foldyna, T. A. Germer, B. C. Bergner, et al., "Generalized ellipsometry of artificially designed line width roughness," *Thin Solid Films*, vol. 519, pp. 2633–2636, 2011.
[57] D. J. Dixit, V. Kamineni, R. Farrell, et al., "Metrology for block copolymer directed self-assembly structures using Mueller matrix-based scatterometry," *J. Nanolithogr. MEMS, MOEMS*, vol. 14, p. 021102, 2015.
[58] P. E. Hansen, M. H. Madsen, J. Lehtolahti, et al., "Traceable Mueller polarimetry and scatterometry for shape reconstruction of grating structures," *Appl. Surf. Sci.*, vol. 421, p. 4719, 2017.
[59] S. Dey, A. Diebold, N. Keller, et al., "Mueller matrix spectroscopic ellipsometry based scatterometry simulations of Si and $Si/Si_xGe_{1-x}/Si/Si_xGe_{1-x}/Si$ fins for sub-7nm node gate-all-around transistor metrology," *Proc. SPIE*, vol. 10585, p. 1058506, 2018.
[60] N. G. Orji, M. Badaroglu, B. M. Barnes, et al., "Metrology for the next generation of semiconductor devices," *Nat. Electron.*, vol. 1, p. 532, 2018.
[61] H. Arwin, R. Magnusson, J. Landin, et al., "Chirality-induced polarization effects in the cuticle of scarab beetles: 100 years after Michelson," *Philos. Mag.*, vol. 92, p. 1583, 2012.
[62] H. Arwin, A. Mendoza-Galván, R. Magnusson, et al., "Structural circular birefringence and dichroism quantified by differential decomposition of spectroscopic transmission Mueller matrices from Cetonia aurata," *Opt. Lett.*, vol. 41, p. 3293, 2016.
[63] O. Arteaga, E. Kuntman, J. Antó, et al., "Mueller matrix microscopy on a Morpho butterfly," *J. Phys. Conf.*, vol. 605, p. 012008, 2015.
[64] V. A. Ushenko, B. T. Hogan, A. Dubolazov, et al., "3D Mueller matrix mapping of layered distributions of depolarisation degree for analysis of prostate adenoma and carcinoma diffuse tissues," *Sci. Rep.*, vol. 11, p. 5162, 2021.
[65] H. Fujiwara, *Spectroscopic Ellipsometry: Principles and Applications*, England, John Wiley & Sons, 2007.
[66] J. J. Gil and R. Ossikovski, *Polarized Light and the Mueller Matrix Approach*, USA, CRC Press, 2016.
[67] R. A. Chipman, "Chapter 14: Mueller matrices," in *Handbook of Optics, Third Edition, Volume 1: Geometrical and Physical Optics, Polarized Light, Components and Instruments(set)*, USA, McGraw-Hill, 2010.
[68] S. R. Cloude and E. Pottier, "A review of target decomposition theorems in radar polarimetry," *IEEE Trans. Geosci. Rem. Sens.*, vol. 34, p. 498, 1996.
[69] R. Ossikovski, M. Anastasiadou, S. Ben Hatit, et al., "Depolarizing Mueller matrices: how to decompose them?" *Phys. Status Solidi*, vol. 205, p. 720, 2008.
[70] S. Y. Lu and R. A. Chipman, "Interpretation of Mueller matrices based on polar decomposition," *J. Opt. Soc. Am. A*, vol. 13, p. 1106, 1996.
[71] R. M. A. Azzam, "Propagation of partially polarized light through anisotropic media with or without depolarization: a differential 4×4 matrix calculus," *J. Opt. Soc. Am.*, vol. 68, p. 1756, 1978.
[72] O. Arteaga and B. Kahr, "Characterization of homogeneous depolarizing media based on Mueller matrix differential decomposition," *Opt. Lett.*, vol. 38, p. 1134, 2013.
[73] H. Arwin, S. Schoeche, J. Hilfiker, et al., "Optical chirality determined from Mueller matrices," *Appl. Sci.*, vol. 11, p. 6742, 2021.
[74] R. Ossikovski, "Differential matrix formalism for depolarizing anisotropic media," *Opt. Lett.*, vol. 36, p. 2330, 2011.
[75] R. Ossikovski, "Differential and product Mueller matrix decompositions: a formal comparison," *Opt. Lett.*, vol. 37, p. 220, 2012.
[76] H. G. Tompkins and J. N. Hilfiker, *Spectroscopic Ellipsometry: Practical Application to Thin Film Characterization*, USA, Momentum Press, 2016.
[77] H. G. Tompkins and E. A. Irene, *Handbook of Ellipsometry*, USA, William Andrew Inc., 2005.
[78] M. Korde, S. Kal, C. Alix, et al., "Nondestructive characterization of nanoscale subsurface features fabricated by selective etching of multilayered nanowire test structures using Mueller matrix spectroscopic ellipsometry based scatterometry," *J. Vac. Sci. Technol. B, Nanotechnol. Microelectron. Mater. Process. Meas. Phenom.*, vol. 38, p. 024007, 2020.
[79] D. J. Dixit, N. Keller, Y. Lifshitz, et al., "Nonconventional applications of Mueller matrix-based scatterometry for advanced technology nodes," *J. Nanolithogr. MEMS MOEMS*, vol. 17, p. 034001, 2018.
[80] D. J. Dixit, S. O'Mullane, S. Sunkoju, et al., "Sensitivity analysis and line edge roughness determination of 28-nm pitch silicon fins using Mueller matrix spectroscopic ellipsometry-based optical critical dimension metrology," *J. Nanolithogr. MEMS MOEMS*, vol. 14, p. 031208, 2015.
[81] R. H. Muller, "Definitions and conventions in ellipsometry," *Surf. Sci.*, vol. 16, p. 14, 1969.
[82] *Cholesteric Liquid Crystal was Prepared by M. Hartveit, W. Zhang, M. Anthamatten, and C. Shaw*, University of Rochester.
[83] J. Wade, J. N. Hilfiker, J. R. Brandt, et al., "Natural optical activity as the origin of the large chiroptical properties in π-conjugated polymer thin films," *Nat. Commun.*, vol. 11, p. 6137, 2020.
[84] O. Arteaga, "Natural optical activity vs circular Bragg reflection studied by Mueller matrix ellipsometry," *Thin Solid Films*, vol. 617, p. 14, 2016.
[85] E. D. Palik, Ed., *Handbook of Optical Constants of Solids II*, USA, Academic Press, 1991, pp. 899–918.
[86] A. Laskarakis, S. Logothetidis, S. Kassavetis, et al., "Surface modification of poly (ethylene terephthalate) polymeric films for flexible electronics applications," *Thin Solid Films*, vol. 516, p. 1443, 2008.
[87] J. N. Hilfiker, B. Pietz, B. Dodge, et al., "Spectroscopic ellipsometry characterization of coatings on biaxially anisotropic polymeric substrates," *Appl. Surf. Sci.*, vol. 421, p. 500, 2017.

Bionotes

James N. Hilfiker
J.A. Woollam Company, 311 South 7th St., Lincoln, NE, 68508, USA
jhilfiker@jawoollam.com
https://orcid.org/0000-0002-4874-5429

James N. Hilfiker received his M.S. in Electrical Engineering at the University of Nebraska in 1995, where he studied under John Woollam. His graduate research involved in-situ ellipsometry applied to both sputter-deposition and electrochemical reactions, and optical characterization of magneto-optic thin films. He joined the J.A. Woollam Company upon graduation, where his research has focused on new applications of ellipsometry, including characterization of anisotropic materials, liquid crystal films, thin film photovoltaics, and Mueller matrix optical characterization. He has authored over 60 technical articles involving ellipsometry, including Encyclopedia articles and four book chapters on topics as varied as vacuum ultraviolet ellipsometry, in-situ spectroscopic, and dielectric function modeling. In 2015, James co-authored the book titled “Spectroscopic Ellipsometry: Practical application to thin film characterization.”

Nina Hong
J.A. Woollam Company, 311 South 7th St., Lincoln, NE, 68508, USA

Nina Hong, received her Ph.D. in physics at the University of Nebraska-Lincoln. She holds Bachelor’s and Master’s degrees in physics from Hanyang University in South Korea. Her research focused on room-temperature solid-state neutron detectors using boron-rich carbon thin films. Her graduate research involved material characterization using AES, XPS, XRD, XRR, IR/Raman Spectroscopy, AFM/MFM, and IV/CV measurements. Nina joined the J.A. Woollam Company in July 2012, where she has been working extensively with anisotropic materials characterization using Mueller matrix spectroscopic ellipsometry. Her recent research focuses are developing ellipsometry solutions for flexible optical devices, anisotropic crystals, and metamaterials.

Stefan Schoeche
J.A. Woollam Company, 311 South 7th St., Lincoln, NE, 68508, USA

Stefan Schoeche, received his Diploma in semiconductor physics from the University of Leipzig, Germany, before moving to Nebraska to get his Ph.D. in Engineering in the ellipsometry research group of Prof. Mathias Schubert. He has extensive experience in thin film deposition including PLD, PVD, and ALD and thin film characterization using XRD, SPM, SEM, Hall, CV/IV, Raman, PL/CL, and photocurrent spectroscopy. His graduate research focused on free-charge carrier and phonon mode properties in group-III nitrides studied by infrared spectroscopic ellipsometry and THz-optical Hall effect, as well as a theoretical description of the optical response of 2D carrier gases at long wavelengths. Stefan joined the Woollam Company in 2014, where he worked as an R&D engineer with responsibility for exploring new instrumentation, applications of ellipsometry, and analysis software improvement. He provides customer support for THz and infrared applications, advanced modeling including nonplanar structures, and measurements with external electric and magnetic fields. Stefan recently accepted an offer to join IBM Research in Albany, NY, as a metrology engineer where his focus will be on OCD and other optical metrology techniques.